



**HAL**  
open science

## Time-resolved Raman and luminescence spectroscopy of synthetic REE-doped hydroxylapatites and natural apatites

Michel Gauthier, Amaury Fau, Olivier Beyssac, Gérard Panczer, Olivier Gasnault, Pierre-Yves Meslin, Sylvain Bernard, Sylvestre Maurice, Olivier Forni, Jean-Claude Boulliard, et al.

### ► To cite this version:

Michel Gauthier, Amaury Fau, Olivier Beyssac, Gérard Panczer, Olivier Gasnault, et al.. Time-resolved Raman and luminescence spectroscopy of synthetic REE-doped hydroxylapatites and natural apatites. *The American Mineralogist*, 2022, 107 (7), pp.1341 - 1352. 10.2138/am-2022-8006 . hal-03775744v2

**HAL Id: hal-03775744**

**<https://hal.science/hal-03775744v2>**

Submitted on 13 Sep 2022 (v2), last revised 19 Nov 2022 (v3)

**HAL** is a multi-disciplinary open access archive for the deposit and dissemination of scientific research documents, whether they are published or not. The documents may come from teaching and research institutions in France or abroad, or from public or private research centers.

L'archive ouverte pluridisciplinaire **HAL**, est destinée au dépôt et à la diffusion de documents scientifiques de niveau recherche, publiés ou non, émanant des établissements d'enseignement et de recherche français ou étrangers, des laboratoires publics ou privés.

1 *Revision #2* *Word counts (all included) 10551, 11 figures, 2 tables*

2

3 **Time-resolved Raman and luminescence spectroscopy of synthetic REE-**  
4 **doped hydroxylapatites and natural apatites**

5

6 Fau A.<sup>(1)</sup>, Beyssac O.<sup>(1),\*</sup>, Gauthier M.<sup>(1)</sup>, Panczer G.<sup>(2)</sup>, Gasnault O.<sup>(3)</sup>, Meslin P.Y.<sup>(3)</sup>, Bernard  
7 S.<sup>(1)</sup>, Maurice S.<sup>(3)</sup>, Forni O.<sup>(3)</sup>, Boulliard J.C.<sup>(1)</sup>, Bosc F.<sup>(4)</sup> and Drouet C.<sup>(4)</sup>

8

9 *(1) IMPMC, UMR 7590 CNRS - Sorbonne Université - MNHN, Campus Jussieu, Case Courrier 115, 4 place*  
10 *Jussieu, F-75005 Paris (2) ILM, UMR5306 - UCBL – CNRS, 10 rue Ada Byron, F-69622 Villeurbanne (3) IRAP,*  
11 *UMR 5277 CNRS - Université Paul Sabatier Toulouse - CNES, 9 Avenue du Colonel Roche, F-31400 Toulouse*  
12 *(4) CIRIMAT, UMR 5085 CNRS - Université Paul Sabatier Toulouse - INP Toulouse, 4 allée Emile Monso*  
13 *F-31030 Toulouse*

14 *\* Corresponding author : [Olivier.Beyssac@upmc.fr](mailto:Olivier.Beyssac@upmc.fr)*

15

16 **Abstract**

17 Using continuous and time-resolved spectroscopy, we investigate Raman and luminescence signals  
18 from synthetic hydroxylapatites doped with trivalent REE including Dy<sup>3+</sup>, Eu<sup>3+</sup>, Nd<sup>3+</sup>, and Sm<sup>3+</sup>, as  
19 well as REE in natural apatites, with laser excitations at 532 nm and 785 nm. We demonstrate that  
20 time-resolved spectroscopy is an extremely efficient method to tune down the luminescence from  
21 Raman spectra or, alternatively, to investigate the luminescence signal without the interference from  
22 the Raman contribution. Time-resolved luminescence spectroscopy is found to be a powerful  
23 technique for generating specific high-quality luminescence spectra for the REE emission activators in  
24 apatites by using appropriate combinations of delay and gate width for the time synchronization of the  
25 laser pulse and ICCD detector. This allows for the unambiguous detection and identification of the  
26 activators by avoiding the overlapping of various emission signals in the luminescence spectra. This is  
27 particularly useful in the case of natural samples, which often have several activators for  
28 luminescence. In the case of synthetic REE-doped apatites, a quenching process for luminescence due  
29 to activator concentration is seen for Eu<sup>3+</sup> and Sm<sup>3+</sup>, i.e. the higher the concentration, the shorter the  
30 luminescence decay time. The interpretation of luminescence decay time in natural apatites is  
31 promising but more complex because of energy transfers between the various luminescence activators  
32 present in the crystal lattice. Luminescence is a powerful technique for detecting the presence of REE  
33 in apatites down to ppm levels, though quantifying the concentration is still a challenge.

34

35 **Keywords:** apatite, time-resolved spectroscopy, Raman, luminescence, REE

36

## 37 **Introduction**

38 Apatites [ $\text{Ca}_5(\text{PO}_4)_3(\text{F},\text{Cl},\text{OH})$ ] is one of the most common accessory minerals in both  
39 terrestrial rocks and meteorites. They have recently been identified *in situ* on Mars by the  
40 ChemCam LIBS instrument onboard the Curiosity rover (Forni et al. 2020). They are also a  
41 very important component of bones or teeth as well as a primary source of phosphorous for  
42 biological processes. Apatites are sensitive tracers of volatiles and fluid-rock interactions in  
43 metamorphic rocks (Harlov 2015), in magmatic and volcanic rocks (Webster & Piccoli 2015)  
44 as well as in meteorites (McCubbin & Jones 2015). They are important minerals for  
45 thermochronological and geochronological investigations of processes occurring at various  
46 depths and temperatures (Chew & Spikings 2015). Last, but not least, apatite offers an  
47 unusual range of applications in ecology, agronomy, biology, medicine, archeology,  
48 environmental remediation, and materials science (Rakovan & Pasteris 2015; Gomez-Morales  
49 et al. 2013). Therefore, it is important to constantly improve the tools used for the  
50 characterization of the structure and chemistry of apatites. To this aim, vibrational  
51 spectroscopies like infrared and Raman, as well as luminescence spectroscopy, can provide  
52 rich amounts of information. This fact, along with a number of practical advantages,  
53 nowadays make them useful tools when exploring the physico-chemical properties of apatite.

54 Raman spectroscopy is useful for a quick, non-destructive and non-ambiguous  
55 identification of apatites down to the microscale (Antonakos et al. 2007). In addition, Raman  
56 spectroscopy provides valuable information on the presence of OH<sup>-</sup> in the halogen site and,  
57 more generally, on the type of apatite: hydroxyl- versus fluor- versus chlor-apatite  
58 (Antonakos et al. 2007). It can also be used to assess the crystallinity of apatite and to track  
59 possible carbonate incorporation in apatite through  $\text{CO}_3^{2-}$  substitution for  $\text{PO}_4^{3-}$  tetrahedra  
60 (Awonusi et al. 2007, and see Pasteris & Beyssac 2020 and references therein).

61 Laser excitation during Raman analysis may also induce emission of luminescence in  
62 apatite. Luminescence is used here as a generic term describing all kinds of  
63 photoluminescence, e.g., fluorescence, luminescence, or phosphorescence (see Gaft et al.  
64 2015 and Waychunas 2014 for further details). Because the luminescence signal can be  
65 extremely strong, such that it can completely overwhelm the Raman signal, it is often  
66 considered as severely limiting for proper Raman analysis. In some cases, the luminescence  
67 peaks can be so sharp that they actually may be confused with Raman peaks (Lenz et al.  
68 2015). However, in many cases luminescence carries rich and valuable information  
69 complementary to the data acquired using Raman (Gaft et al. 2015; Nasdala et al. 2004;  
70 Panczer et al. 2012; Waychunas 2014). This is particularly the case in apatites (Waychunas

71 2002; Gaft & Panczer 2013). Recent developments in Raman hyperspectral mapping further  
72 allow for the mapping of luminescence patterns in minerals on the microscale, which opens  
73 new avenues for the non-destructive investigation of the internal microtexture of minerals  
74 (Nasdala et al. 2012; Lenz and Nasdala 2015).

75 One possible means of avoiding or limiting luminescence is to change the wavelength  
76 of the laser excitation used for Raman analysis in the range from the deep ultra-violet (UV) to  
77 the near infrared (IR). This approach works well in some cases but it is also limited by severe  
78 analytical challenges (e.g. deep UV) or by the poor Raman efficiency at high wavelength in  
79 the near IR region (Dubessy 2012; Beyssac 2020 for a review). Another possibility is to use  
80 time-resolved (TR) spectroscopy, which utilizes the different lifetimes of the Raman and  
81 luminescence processes. The Raman effect is actually a prompt phenomenon with an  
82 extremely short lifetime ( $\approx 10^{-15}$  s). In contrast, the lifetime of luminescence processes in  
83 minerals is longer, ranging from fractions of nanoseconds to seconds and even more (Panczer  
84 et al. 2012; Gaft et al. 2015). By perfectly synchronizing in the time-domain a pulsed-laser (in  
85 the nanosecond range) with a gated intensified CCD (ICCD), it is possible to excite  
86 effectively the Raman effect and to reject efficiently most of the luminescence especially if it  
87 has a long decay time. Furthermore, time-resolved spectroscopy makes possible the  
88 exploration of the time decay or lifetime of luminescence, which is a measure of the transition  
89 probability between two specific levels. Such a lifetime is then a specific and unique property  
90 of the luminescence signal (Gaft and Panczer 2013) for a given electronic transition in a  
91 precise crystallographic environment.

92 Rare-Earth Elements (REE) are a large and very important group of elements in  
93 mineralogy and geochemistry. REE incorporation in minerals and exchanges of REE between  
94 minerals, melts, and fluids are fundamental in geochemistry and can provide key information  
95 on many geological processes. Since they behave as emission centers in minerals, here called  
96 luminescence activators, the luminescence properties of REE can be used to detect possible  
97 internal zoning in minerals using cathodoluminescence (Waychunas 2014; Gaft et al. 2015) or  
98 photoluminescence (Lenz and Nasdala 2015). Because the apatite structure can accommodate  
99 a large variety of elements (Hughes and Rakovan, 2015), it is a well adapted matrix for  
100 incorporating the REE via two principal coupled substitutions:  $REE + Na = 2Ca$  and  $REE +$   
101  $Si = Ca + P$ . In fossilized bones for example, REE are progressively incorporated in bone  
102 apatite during diagenesis, due to exchange with the surrounding minerals (Suarez et al.,  
103 2010). In the field of nanomedicine, the intentional incorporation of luminescent REE as  
104 dopants in synthetic bioapatites/bone allows for nanoparticle tracking as a form of medical

105 diagnosis (Mondéjar et al., 2007, Al-Kattan et al., 2014). The luminescence signal of REE in  
106 apatite has recently been exploited, coupled to Raman and histology analysis, to follow the  
107 skin penetration of apatite-based colloidal nanoparticles for dermatological applications  
108 (Choimet et al. 2020).

109 Simple yet valuable investigations of luminescence properties in minerals can be done  
110 using a conventionnal Raman spectrometer, an instrument largely accessible nowadays in  
111 laboratories, and even for field studies (Jehlicka et al. 2017). Notably, there are currently  
112 more and more combined Laser-Induced Breakdown Spectroscopy (LIBS) and Raman  
113 investigations often combined in a single instrument (see Fau et al. 2019 and references  
114 therein). LIBS provides the chemistry and Raman determines the mineralogy. LIBS can detect  
115 major and many trace elements but is not able to detect REE at low concentrations.  
116 Luminescence spectroscopy can fill the gap and provide detection of REE for such studies.  
117 This is particularly the case for the SuperCam instrument, which is an instrumental suite  
118 currently deployed on Mars onboard the NASA Perseverance rover. SuperCam combines  
119 remote LIBS and time-resolved Raman and luminescence spectroscopy (Wiens et al. 2021,  
120 Maurice et al. 2021, Beysac 2020).

121 The purpose of the present study is to investigate (i) the structural properties by  
122 Raman spectroscopy and (ii) the luminescence properties, of REE in both synthetic REE-  
123 doped hydroxylapatites (used as standards) as well as natural apatites. In the case of the  
124 synthetic hydroxylapatites, they are doped with trace amounts of one REE, either  $\text{Eu}^{3+}$ ,  $\text{Sm}^{3+}$ ,  
125  $\text{Nd}^{3+}$  or  $\text{Dy}^{3+}$ . We also document the decay time of the luminescence signal vs. the  
126 concentration of the specific REE. The case of natural apatites is more complex to interpret  
127 since several emission centers for luminescence are present within a given sample.  
128 Comparison of the time-resolved luminescence spectra between synthetic and natural apatites  
129 is first discussed in order to interpret the peaks in the luminescence emission spectra. In  
130 addition, we discuss possible factors affecting that the luminescence signal of REE in apatite,  
131 in particular those, which control the evolution of luminescence in the time domain like  
132 quenching and/or sensitizing phenomena.

133

## 134 **An overview on Raman and luminescence in apatite**

135 Apart from a few exceptions, such as end member chlorapatite (monoclinic system, space  
136 group  $P2_1/b$ ), apatites generally crystallize with a hexagonal structure in the  $P6_3/m$  space  
137 group symmetry. The structure contains five crystallographic sites: the Ca1 (9-fold

138 coordination) and Ca2 (7-fold coordination) sites, the P site, the halogen/OH<sup>-</sup> site, and  
139 “defect” sites following the terminology by Waychunas (2002). More details on the topology  
140 of these sites and, more generally, on the crystal structure of apatites may be found in Hughes  
141 and Rakovan (2002, 2015).

142 The apatite Raman spectrum has been extensively described by O'Shea et al. (1974)  
143 and Antonakos et al. (2007). The PO<sub>4</sub><sup>3-</sup> and OH<sup>-</sup> ions in apatite can be easily detected by  
144 Raman (Rey et al. 2014). The most intense Raman peak, often used for a quick detection of  
145 apatite, is located at  $\approx 960\text{ cm}^{-1}$  and is due to the  $\nu_1$  symmetric stretching mode of PO<sub>4</sub><sup>3-</sup>.  
146 Additional peaks due to PO<sub>4</sub><sup>3-</sup> are the doubly degenerate  $\nu_2$  bending mode at  $\approx 430\text{ cm}^{-1}$ , the  
147 triply degenerate antisymmetric  $\nu_3$  stretching mode at  $\approx 1060\text{ cm}^{-1}$ , and the triply degenerate  
148  $\nu_4$  bending mode at  $\approx 580\text{ cm}^{-1}$ . OH<sup>-</sup>, when present, contributes a large band at  $\approx 3570\text{ cm}^{-1}$ ,  
149 while F<sup>-</sup> and Cl<sup>-</sup> can not be directly detected by Raman. However, the presence of F<sup>-</sup> and/or  
150 Cl<sup>-</sup> in the OH<sup>-</sup> site may induce a shift of the various PO<sub>4</sub><sup>3-</sup> vibration modes as well as  
151 modifications in the OH<sup>-</sup> domain due to a modified configuration of hydrogen bonds.

152 Luminescence of apatites has been extensively studied for a long time (Blasse 1975).  
153 Waychunas (2002) and Gaft et al. (2015) made comprehensive reviews while other studies  
154 were dedicated to the specific luminescence resulting from Eu (Kottaisamy et al. 1994; Gaft  
155 et al. 1997), or more generally to the REE luminescence patterns overall (Reisfeld et al. 1996;  
156 Czaja et al. 2010). Other studies have been dedicated to other emission centers in apatite such  
157 as U<sup>6+</sup> and (UO<sub>2</sub>)<sup>2+</sup> (Panczer et al. 1998) or Mn<sup>2+</sup> (Gaft et al. 2015). Waychunas (2002)  
158 provided a detailed description of the luminescence activator types and described their link  
159 with the apatite structure. Each of the five sites in apatite can be occupied by activators, but  
160 the most common ones, *i.e.* those observed in natural apatites, in particular REE or Mn<sup>2+</sup>, go  
161 in the Ca1 and Ca2 sites (Waychunas 2002).

162 Luminescence activators for which the change in configurational coordinate between  
163 the ground and excited state is small, or even null, will generate very narrow emission lines.  
164 This is the case for REE<sup>3+</sup>, for which (i) the parity forbidden  $4f-4f$  transitions should be weak  
165 unless being enhanced by symmetry crystal fields establishing a relationship between  
166 intensity and site symmetry, and (ii) the allowed  $4f-5d$  transitions generally lead to slightly  
167 broader bands. Alternatively, owing to their different localisation within the electronic  
168 structure and difference in symmetries between the ground and excited states, some  
169 transitions will yield emission bands with much larger widths such as the  $d-d$  transitions in  
170 Mn<sup>2+</sup>. Activators generally do not behave independently in the apatite structure and some may

171 transfer part or all of their energy to other nearby activators becoming sensitizers. This applies  
172 to some REE<sup>3+</sup> that can be sensitized by Mn<sup>2+</sup>. This triggers and enhances emission by REE<sup>3+</sup>  
173 and decreases that of Mn<sup>2+</sup> (Marfunin 1979). Conversely, some authors have argued that Eu<sup>2+</sup>  
174 can act as a sensitizer of Mn<sup>2+</sup> luminescence (Knutson et al. 1985; Kottaisamy et al. 1994). Of  
175 course, not only a single but a series of REE are generally present in natural apatites making  
176 very likely the occurrence of transitions with similar energy. This may favor not only single  
177 energy transfer but also multiple ones involving several REE (Waychunas 2002).

178 In natural apatites, REE can easily substitute for Ca via two coupled substitutions  
179 (REE + Na = 2Ca and REE + Si = Ca + P) and become emission centers for luminescence in  
180 the crystallographic structure of the host apatite. REE are incorporated in either the Ca1  
181 and/or Ca2 sites and can be luminescent as trivalent or divalent ions. When trivalent REE ions  
182 are incorporated in substitution of Ca along with Na or Si (Hosseini et al., 2014), this may  
183 generate “abnormalities” or defects in the apatitic lattice altering the local site symmetry  
184 (which could have an impact on the luminescence). Studies using steady-state luminescence,  
185 *i.e.* continuous excitation in the time domain, generally via UV excitation, have demonstrated  
186 that natural apatite luminescence is dominated by divalent Mn<sup>2+</sup> and Eu<sup>2+</sup> and trivalent Ce<sup>3+</sup>,  
187 Dy<sup>3+</sup>, Nd<sup>3+</sup>, and Sm<sup>3+</sup> (Gaft et al. 2001). The particular case of Eu substitution in apatite has  
188 been extensively studied by Gaft et al. (1997, 2001) and Kottaisamy et al. (1994). These  
189 studies give an overview regarding the complexity of REE luminescence in apatite but also  
190 provide a great deal of information with respect to this technique. In apatite, Eu<sup>2+</sup>  
191 luminescence appears as a single band at  $\approx$  450 nm due to a  $4f-5d$  transition with a lifetime of  
192 500 ns (Gaft et al. 2001). It has been assigned to the Ca2 site by Kottaisamy et al. (1994).  
193 Eu<sup>3+</sup> luminescence is characterized by lines at 590, 617, 651 and 695 nm and was assigned to  
194 the Ca1 site (Gaft et al. 2001). In synthetic Eu-doped apatites under a specific excitation,  
195 additional lines were observed at 575, 628 and 712 nm and were assigned to Eu<sup>3+</sup> in the Ca2  
196 site (Morozov et al. 1970).

197

## 198 **Synthetic and natural apatite samples**

### 199 ***REE-doped synthetic hydroxylapatites***

200 REE-doped hydroxylapatites were synthesized at CIRIMAT Toulouse at relevant geological  
201 concentrations, following the method described by Hosseini et al. (2014). The REE selected  
202 for this study are trivalent Eu<sup>3+</sup>, Sm<sup>3+</sup>, Nd<sup>3+</sup>, and Dy<sup>3+</sup> because they are important geochemical  
203 tracers and their luminescence patterns in apatite is known. We selected trivalent REE  
204 because they emit luminescence in spectral windows relevant to our instrumental setup and

205 they are also observed in natural samples. The high-purity REE salts used were purchased  
206 from SIGMA-ALDRICH. First, we prepared a stock solution of each REE doping element  
207 with a concentration of 0.04 mol/L by dissolving respectively europium(III) chloride  
208 hexahydrate, ( $\text{EuCl}_3 \cdot 6\text{H}_2\text{O}$  – molecular weight MW: 366.41 g/mol), samarium(III) nitrate  
209 hexahydrate, ( $\text{Sm}(\text{NO}_3)_3 \cdot 6\text{H}_2\text{O}$  - MW: 444.47 g/mol), dysprosium(III) chloride hexahydrate,  
210 ( $\text{DyCl}_3 \cdot 6\text{H}_2\text{O}$  - MW: 376.95 g/mol) and neodymium(III) nitrate hexahydrate,  
211 ( $\text{Nd}(\text{NO}_3)_3 \cdot 6\text{H}_2\text{O}$  - MW: 438.35 g/mol) in deionized water. Preparation of hydroxylapatites  
212 was based on coprecipitation obtained by mixing two starting solutions. Solution A contained  
213 calcium nitrate tetrahydrate ( $\text{Ca}(\text{NO}_3)_2 \cdot 4\text{H}_2\text{O}$  - MW: 236.15 g/mol) dissolved in deionized  
214 water to obtain a Ca concentration of 0.4 mol/L. Solution B contained di-ammonium  
215 hydrogenphosphate ( $(\text{NH}_4)_2 \cdot \text{HPO}_4$  - MW: 132.06 g/mol) dissolved in deionized water at a  
216 phosphate concentration of 0.13 mol/L. REE-doped hydroxylapatites at desired  
217 concentrations of the doping element were obtained by mixing solutions A and B and the  
218 relevant REE stock solution diluted as necessary and to which 2 mL of 30%  $\text{NH}_4\text{OH}$   
219 ammonia were added to increase the pH of the solution in order to facilitate the  
220 hydroxylapatite precipitation. The obtained mixtures are then placed in an oven at 143 °C for  
221 a duration of 14 hours. Three successive washing stages with deionized water and  
222 centrifugation for 3 minutes at 7500 rpm were carried out in order to remove traces of  
223 ammonia and unreacted salts present in the precipitating medium. Finally, the samples were  
224 dried in an oven at 80 °C for a minimum of 8 hours.

225

### 226 *Natural apatites*

227 The natural apatites (mm to cm in size) were selected from the collection de Minéraux  
228 (Sorbonne Université, Paris). Table 1 summarizes the main information for each apatite  
229 specimen used. These samples are either single crystals or polycrystalline aggregates.

230

## 231 **Methodology**

### 232 *Chemical analyses*

233 Major and trace element analyses for natural and synthetic apatites were done by alkali fusion  
234 of rock samples ( $\text{LiBO}_2$ ), followed by concentration measurements using an ICP-OES Icap  
235 6500 (Thermoscientific) for major elements, and an ICP-MS X7 (Thermoscientific) for trace  
236 elements (protocol by Carignan et al., 2001). Analyses were performed at the Service  
237 d'Analyse des Roches et Minéraux (SARM, CNRS, Nancy, France). For the  $\text{Dy}^{3+}$ -doped  
238 synthetic apatite, chemical analysis was performed on only one sample as a luminescence



239 signal was not detected for these samples (see below). Table 1 and Table 2 present the major  
240 (oxide wt%) and trace element (mg/g) composition of the natural and synthetic REE doped  
241 samples, respectively. Figure 1 depicts the chondrite normalized REE patterns for the natural  
242 apatites.

243

#### 244 *X-ray diffraction*

245 XRD was used to confirm the crystallography of the synthetic apatites prepared. We used a  
246 Panalytical Pro MPD operating at 40 kV, 40 mA with Co-K $\alpha$  radiation wavelength of  $\lambda =$   
247 1.788965 Å. Diffractograms were recorded from 5 to 90° in a 2 $\theta$  scale and 0.033° step size  
248 during 3 cycles of 1.5 hour.

249

#### 250 *Infrared spectroscopy*

251 Fourier transform infrared (FTIR) was used to characterize and verify the crystallinity and  
252 molecular structure of the synthetic apatites. We used a Nicolet Magna 560 working under  
253 dry air. All measurements were done in transmission mode with a Globar / Nernst lamp  
254 source and a DTGS-CsI detector. Spectra were obtained in the 4000-400 cm<sup>-1</sup> range with a  
255 resolution of 2 cm<sup>-1</sup> and by averaging 200 spectra. Before analyses, samples were prepared by  
256 mixing 1 mg of REE-doped hydroxylapatite with 300 mg of dried KBr which was then  
257 pressed into pellets and dried at 120°C.

258

#### 259 *Continuous-wave Raman spectroscopy*

260 All samples were analyzed using a continuous-wave Raman microspectrometer Renishaw  
261 InVia Reflex for point analyses and Raman hyperspectral mapping when needed.  
262 Measurements were performed using a green 532 nm solid-state laser focused on the sample  
263 through a Leica DM2500 microscope with a long-working distance 50X objective (NA =  
264 0.55). This configuration yields a planar resolution of approximately 1-2  $\mu\text{m}$  for a laser power  
265 delivered at the sample surface of less than 1 mW using neutral density filters to prevent  
266 irreversible thermal damage. This corresponds to a laser irradiance in the range of 0.3 to 1.3  
267 10<sup>9</sup> Wm<sup>-2</sup>. All measurements were performed with a circularly polarized laser using a 1/4-wave  
268 plate placed before the microscope in order to minimize polarization effects. The Raman  
269 signal was dispersed by a grating with 2400 lines/mm and the signal was analyzed with a  
270 RENCAM CCD detector. The spectral resolution for visible light was 1 to 1.9 cm<sup>-1</sup> and the  
271 wavenumber accuracy was better than 0.5 cm<sup>-1</sup>. Some samples (Nd<sup>3+</sup>-doped hydroxylapatites)

272 were also analyzed using a 785 nm diode laser yielding a spot size of a few  $\mu\text{m}^2$  for excitation  
273 and a 1200 lines/mm grating for dispersion. The rest of the setup was the same.

274 For Raman mapping and the acquisition of hyperspectral maps, the sample was moved  
275 with an appropriate step size using a XYZ Renishaw motorized stage. Laser focus was  
276 optimized by correcting topographic variation prior to analysis (surface mode using the  
277 Renishaw Wire 4.3 software) and all maps were processed using the Wire 4.3 software. More  
278 details concerning the Raman mapping technique can be found in Bernard et al. (2008). All  
279 measurements were performed at room temperature and spectra were recorded directly on the  
280 raw samples without any preparation. Note that continuous-wave Raman spectroscopy also  
281 provides steady-state luminescence emission spectra in the range 532-720 nm with excitation  
282 at 532 nm, or in the range 785-930 nm with excitation at 785 nm.

283

#### 284 *Time-resolved Raman and luminescence spectroscopy*

285 All samples were also analyzed using a custom-built, time-resolved Raman and luminescence  
286 spectrometer as described by Fau et al. (2019). The laser is a nanosecond (1.2 ns FWHM, 1  
287 mJ per pulse) pulsed, diode-pumped, solid-state (DPSS) laser operating at 532 nm with a 10  
288 to 2000 Hz repetition rate. The laser is slightly defocused at the sample surface through a  
289 microscope objective (MPlan Apo Mitutoyo 20X, NA= 0.42). The Raman and luminescence  
290 signals are collected using a backscattering geometry. In addition, the laser was circularly  
291 polarized thanks to a  $\frac{1}{4}$ -wave plate placed before the microscope in order to minimize  
292 polarization effects. In this setup, a Notch filter cut off the Rayleigh scattering at  $\approx 90 \text{ cm}^{-1}$ .  
293 The signal was collected using an optical fiber and sent into a modified Czerny-Turner  
294 spectrometer (Princeton Instruments IsoPlane 320) coupled with an intensified Princeton  
295 Instruments PIMAX4 ICCD camera. The fine control of both the time delay and the gating  
296 time of the camera allows for sub-nanosecond time resolution experiments thanks to a precise  
297 synchronization between the laser pulse and the ICCD. This spectrometer has three motorized  
298 gratings, which can be selected depending on the spectral window and resolution required for  
299 the measurement. In this study, we mostly used a 600 lines/mm grating yielding a spectral  
300 resolution of 10-13  $\text{cm}^{-1}$ . Irradiance, associated with a pulsed laser, can be estimated as  
301  $Q/(\tau S)$ , with  $Q = P/f$  being the laser energy per pulse,  $P$  being the time-integrated laser power  
302 measured at the surface of the sample,  $f$  the laser repetition rate,  $\tau$  the pulse duration, and  $S$   
303 the surface area of the laser spot on the sample. For these experiments, irradiance was set at  $\approx$   
304  $10^{10} \text{ Wm}^{-2}$ , which is a conservative value even in the case of absorbing minerals (Fau et al.  
305 2019).

306

### 307 **Time-resolved Raman and luminescence spectroscopy: overview**

308 The luminescence signal is generally much stronger than the extremely weak Raman signal.  
309 One way to separate the Raman signal from the luminescence signal is to exploit the fact that  
310 these two processes have very different lifetimes using time-resolved spectroscopy. Lifetime  
311 corresponds to the time spent in any excited state, *i.e.* vibrational for Raman and electronic  
312 for luminescence, before it returns to the ground state. For luminescent compounds, de-  
313 excitation is expected to occur by the emission of a photon. However, depending on the  
314 energy gap between the excited and ground states of a given luminescent center (e.g.  $\text{Eu}^{3+}$  or  
315  $\text{Tb}^{3+}$  ions), de-excitation may partially also occur by a non-radiative process such as in the  
316 form of vibrational energy (phonon) if a good energetic correspondence is found. This has  
317 been reported in apatites with O-H vibrations (Al-Kattan et al., 2014). However, even in this  
318 case, luminescent signals remain strong. In all cases, light absorption is “immediate” in the  
319 range of  $10^{-18}$  seconds, while Raman and the emission of luminescence are longer processes.  
320 Relaxation from virtual vibrational levels is typically in the range of  $10^{-15}$  seconds for Raman  
321 and can be considered as “immediate” on our experimental time scale. On the other hand,  
322 going back from excited electronic levels to the ground state is a much slower process, such  
323 that the lifetime of luminescence can cover a wide time range from the nanosecond (e.g.,  
324 organic fluorescence, Lakowicz 2006) to milliseconds or even seconds (e.g.,  $\text{Cr}^{3+}$  or  $\text{REE}^{3+}$  in  
325 minerals, Gaft et al. 2015).

326 Time-resolved spectroscopy uses a pulsed excitation signal synchronized with a gated  
327 detector. The main idea is that the Raman signal will last only during the excitation pulse,  
328 while the luminescence will be excited within the pulse but will continue to emit and decay  
329 after the pulse. Using a short time gate perfectly synchronized with the laser pulse and  
330 matching it in the time domain allows for rejection of most of the luminescence signal and the  
331 maximization of the collection of the Raman signal. Time-resolved spectroscopy further  
332 allows for the collection of only the luminescence signal, without any Raman contribution, by  
333 simply opening the detector gate just after the laser pulse. The Raman signal has then  
334 completely vanished and is absent in the spectrum while the luminescence is still present.

335 In this study, we investigate the emission spectra, which were obtained with an incident  
336 excitation laser at 532 nm, or 785 nm in the case of  $\text{Nd}^{3+}$  using the continuous-wave  
337 spectrometer. Such excitation wavelengths are likely not optimal for triggering absorption and  
338 thereby emission of luminescence. Using UV would be more efficient, but these wavelengths  
339 constitute a good compromise for combining Raman and luminescence investigations. The

340 custom-built time-resolved instrument used for this study offers an excellent synchronization  
341 making possible the exploration of luminescence with various lifetimes. To this aim, an  
342 appropriate combination of delays (the moment the detector gate opens with respect to the  
343 laser pulse) and the gate width has to be used.

344 Lastly, this technique allows for the proper characterization of the decay time of the  
345 luminescence by doing time sweep experiments. A post-pulse detector gate with an  
346 appropriate opening duration is shifted for various time delays, and the integrated intensity of  
347 the signal can be plotted versus the shift time (delay). These data allow for the lifetime to be  
348 calculated and give further information on the nature of the electronic transition and, more  
349 practically, on the identification of the emission center (Lakowicz 2006; Gaft & Panczer  
350 2013; Gaft et al. 2015).

351 Luminescence decay is given by

$$352 \quad I(t) = I_0 e^{-\frac{t-t_0}{\tau}} \quad (1)$$

353 with  $I_0$  being the number of photons emitted at time  $t_0$ , and  $\tau$  the lifetime of the considered  
354 transition. Analysis of the luminescence decay is done by measuring the number of photons  
355 received during a period of time controlled by the gate width and by shifting this gate through  
356 time after the laser pulse. Critical parameters are then the gate width  $t_g$  and the time  
357 increment  $t_s$  by which the gate is shifted.

358 Using the time-resolved setup one effectively measures:

$$359 \quad F(T) = \int_T^{T+t_g} I_0 e^{-\frac{t-t_0}{\tau}} dt \quad (2)$$

360 in  $n+1$  points given by

$$361 \quad T_k = t_0 + k t_s \quad (3)$$

362 After normalisation by the gate width and the introduction of equation (3),  $F(T)$  becomes

$$363 \quad F(T_k) = I_0 t_g e^{-\frac{k t_s}{\tau}} \left( \frac{1 - e^{-\frac{t_g}{\tau}}}{\frac{t_g}{\tau}} \right) \quad (4)$$

364 Several aspects about the methodological information can be retrieved from this equation.  
365 First, the gate width does not influence the experimental evaluation of  $\tau$  because whatever the

366 value of  $\tau$ ,  $\left( \frac{1 - e^{-\frac{t_g}{\tau}}}{\frac{t_g}{\tau}} \right)$  is a constant value even if  $\frac{t_g}{\tau}$  is large. For a reliable assesment of  $\tau$ ,

367 luminescence must have decayed notably so that  $\frac{k t_s}{\tau} > \frac{1}{4}$ . To have an acceptable uncertainty,

368 the statistics have to be good, and so the  $k$  value has to be large. Lastly, the unpredictable

369 factor is the intensity of the luminescence. The lower the intensity, the larger the signal

370 accumulation time required to obtain a correct spectrum. This is an important parameter to  
371 consider in such experiments, which has an important effect on the duration of the decay time  
372 experimental analysis (time sweep experiment).

373 To exploit efficiently the luminescence spectra and the time sweep experiments, a specific  
374 script was written using Python. A Voigt function is used for fitting all peaks and includes a  
375 Gaussian component with a fixed FWHM value at  $13\text{ cm}^{-1}$  corresponding to the instrument  
376 resolution and a Lorentzian component due to the luminescence signal. A linear baseline  
377 defined by two points, automatically calculated as the lowest points from a predefined region  
378 in the spectrum, was subtracted prior to the luminescence peak fitting. No normalization was  
379 performed before data processing. For each time sweep experiment, the selected peaks were  
380 fitted on the first spectrum of each series, when the signal-to-noise ratio is high, by leaving  
381 free the Lorentzian FWHM as well as the area and position of the Voigt band. A second series  
382 fit is then performed on the whole series of spectra with just the Voigt band area as a free  
383 parameter. Lifetime is determined from the semi-logarithmic representation of the intensity  
384 versus time delay and is taken as the slope of the regression line extracted from the  
385 experimental points.

386 In addition, time-resolved spectroscopy allows for the exciting selection of  
387 luminescence emissions from various emission centers if they have different decay lifetimes.  
388 This is a very promising approach for the interpretation of luminescence spectra, especially in  
389 the case of apatites, since emission peaks from various emission centers often overlap in the  
390 spectral domain.

391

## 392 **Results**

### 393 *Physico-chemical characterisation of the REE-doped synthetic apatites*

394 XRD diffractograms of synthetic hydroxylapatites display all the main characteristic peaks of  
395 hydroxylapatite thus confirming their crystallinity (Figure 2). These findings are corroborated  
396 by FTIR spectroscopic analyses (Figure 3). All the infrared spectra obtained are very similar  
397 for the different synthetic hydroxylapatites and exhibit the spectral features characteristic of  
398 hydroxylapatite (Rey et al., 2014). This is seen in the presence of an  $\text{OH}^-$  peak at  $3570\text{ cm}^{-1}$   
399 (O-H stretching) and an associated libration band at  $632\text{ cm}^{-1}$ . The presence of trace  
400 impurities in the form of nitrate  $\text{NO}_3^-$  ions is detectable as a minor contribution ( $\approx 1383\text{ cm}^{-1}$ ).  
401 In addition, the presence of  $\text{H}_2\text{O}$  in the synthetic apatites is detectable via a wide band due to  
402 the vibration of  $\text{H}_2\text{O}$  molecules at around  $3400\text{ cm}^{-1}$ .

403 Chemical data obtained for the major and trace elements in the synthetic  
404 hydroxylapatites are presented in Table 1. Table 1 shows that the range of concentrations  
405 obtained for  $\text{Eu}^{3+}$ ,  $\text{Sm}^{3+}$ ,  $\text{Dy}^{3+}$ , and  $\text{Nd}^{3+}$  varies from tens to thousands of ppm. However, the  
406 luminescence signal for  $\text{Dy}^{3+}$  was not detected (see below). We also note that some  
407 hydroxylapatites were slightly contaminated by another REE than the one used for the  
408 synthesis. This is likely due to impurities in the REE salts used in the synthesis. For instance,  
409 the sample of hydroxylapatite doped with a concentration of 24 ppm of Sm also has a Eu  
410 concentration of around 5 ppm. Continuous-wave Raman mapping was performed on some of  
411 the synthetic hydroxylapatites in order to assess their homogeneity by obtaining thousands of  
412 spectra from a given sample. These maps showed that the chemical composition of these  
413 samples is homogeneous because the FWHM and peak position of the main  $\nu_1$  peak is  
414 constant with only minor variations ( $<1 \text{ cm}^{-1}$ ).

415

#### 416 *Time-resolution Raman spectroscopy*

417 Figure 4 depicts representative continuous-wave micro-Raman spectra obtained at random  
418 positions on the synthetic hydroxylapatites. The Raman signal remains constant in the Raman  
419 shift for all the synthetic hydroxylapatites, while the luminescence emission after light  
420 absorption strongly depends on the excitation wavelength for each REE.  $\text{Eu}^{3+}$  ions are highly  
421 excited at 532 nm and luminescence completely masks the Raman signal (Figure 4a) while for  
422  $\text{Sm}^{3+}$  luminescence is less strong and the Raman signal is visible (Figure 4b). In the case of  
423  $\text{Dy}^{3+}$ -doped apatites, 532 nm is out of the range of absorption (excitation) and emission of  
424 luminescence is not observed while the Raman bands are plainly visible (Figure 4c). Note that  
425 the case of  $\text{Nd}^{3+}$  is different. Raman peaks are clearly visible when excited at 532 nm but non-  
426 visible with excitation at 785 nm because the luminescence of  $\text{Nd}^{3+}$  is extremely strong in the  
427 near IR region (Figure 4d).

428 Figure 5 shows a representative Raman spectrum obtained with the time-resolved  
429 Raman instrument with a short gate (5 ns) centered on the laser pulse. This spectrum was  
430 obtained with a highly luminescent hydroxylapatite doped with 23,936 ppm  $\text{Sm}^{3+}$ . Similar  
431 spectra were obtained for all the other synthetic doped hydroxylapatites. The difference is  
432 striking with continuous-wave Raman spectroscopy as no luminescence bands are detected  
433 while all the Raman peaks are clearly visible, including the OH<sup>-</sup> bands. This is due to the  
434 efficient rejection of the longer lasting REE luminescence.

435 The case for natural apatites is more complex when analyzed with continuous-wave  
436 Raman spectroscopy (Figure 6). A very strong background, including some peaks due to

437 Raman and luminescence, is observed in all the spectra. In general, only the main  $\nu_1$   
438 symmetric stretching mode of  $\text{PO}_4^{3-}$  is observed in all these these spectra while the other  
439 stretching modes are hardly detected in some of the samples (Slyudyanka and Imilchil).  
440 Clearly, using time-resolved Raman spectroscopy makes possible the rejection of almost all  
441 the luminescence contributions in these natural apatites and the recording of high-quality  
442 Raman spectra without any luminescence interference. It is particularly interesting in the case  
443 of the REE because they generate intense, thin peaks that can be easily confused with Raman  
444 peaks in phosphate minerals but also in other mineral phases like zircon as discussed by Lenz  
445 et al. (2015).

446 In the REE-doped synthetic hydroxylapatites, the Raman shift of the  $\nu_1$  symmetric  
447 stretching mode of  $\text{PO}_4^{3-}$  is nearly constant at about  $960 \pm 1 \text{ cm}^{-1}$ . In the natural apatites, this  
448  $\text{PO}_4^{3-}$  mode is in the range 963.8 to 965.4  $\text{cm}^{-1}$ . A strong OH<sup>-</sup> band is observed in all the  
449 synthetic apatites while it is not observed in the natural apatites, nor in the time-resolved  
450 Raman spectra. The Raman shift of the  $\nu_1$  symmetric stretching mode for  $\text{PO}_4^{3-}$  is actually  
451 sensitive to the nature of the apatite (Ashley et al. 2018). It occurs at  $\approx 960 \text{ cm}^{-1}$  in pure  
452 hydroxylapatite,  $\approx 961 \text{ cm}^{-1}$  in pure chlorapatite, and  $\approx 965 \text{ cm}^{-1}$  in pure fluorapatite. This is  
453 due to the fact that Cl<sup>-</sup> has a much larger ionic radius compared to F<sup>-</sup>. From these  
454 observations, Raman investigations confirmed that the synthetic apatites are pure  
455 hydroxylapatites as assessed from infrared and XRD characterization. The natural apatites are  
456 solid solutions in between the three endmembers (OH<sup>-</sup>-Cl<sup>-</sup>-F<sup>-</sup> apatites), though the Raman  
457 spectra do not show a notable contribution of OH<sup>-</sup> (Figure 6). Based on the Raman shift of  
458 the  $\nu_1$  symmetric stretching mode of  $\text{PO}_4^{3-}$ , most natural samples appear to have Raman shift  
459 values corresponding to high levels of F<sup>-</sup> in the halogen site and these samples likely  
460 correspond essentially to fluorapatites. Only the case of the Imilchil sample is slightly  
461 different with a lower shift and this sample has likely a higher Cl<sup>-</sup> level in the halogen site.

462

## 463 **Discussion**

### 464 *Time-resolved luminescence for detecting REE and other emission centers*

465 If time-resolved spectroscopy allows for luminescence features in Raman spectra to be  
466 eliminated, it can also eliminate the Raman contribution from luminescence spectra. In order  
467 to accomplish this, the ICCD gate has to be opened after the laser pulse when the Raman  
468 signal is no longer active. For many minerals, including apatite, the main luminescence

469 emission lines can be assigned rather confidently unless there is a strong overlap between the  
470 various luminescence signals, which then makes the interpretation complex (Gaft et al. 2015).

471 In the natural apatites, the total Raman and luminescence spectra obtained using  
472 continuous-wave illumination is actually not straightforward to interpret (Figure 6). This is due  
473 to the multiple emission lines of the various REE incorporated in the mineral structure (Figure  
474 1) in addition to the possible contribution from other activators like  $\text{Mn}^{2+}$ .  $\text{Mn}^{2+}$  is actually  
475 likely partly responsible for the broad background observed in some of the natural apatites.  
476 Figure 7 illustrates the capability of time-resolved spectroscopy to separate the Raman signal  
477 from the luminescence signal in the Durango apatite. In addition, this technique allows further  
478 investigations of the luminescence by generating spectra specific to activators with various  
479 lifetimes by selecting appropriate combinations of delays and gates. In the case of the  
480 Durango apatite (Figure 7), this technique allows for the retrieval of a clear spectrum from the  
481 short-lifetime luminescence signal due to  $\text{Er}^{3+}$  by opening a short gate (1,500 ns) just after the  
482 laser pulse (delay 6 ns). Erbium luminescence is otherwise completely covered by longer  
483 lifetime emissions in the continuous wave emission spectrum. In a complementary approach,  
484 this technique allows for analysis of long lifetime emissions by opening a wide gate (450,000  
485 ns) long after the laser pulse (delay 1,500 ns). Ideally, if activators are expected in a given  
486 sample and the approximative lifetime of their emission is known, appropriate combinations  
487 of delay and gate should allow for maximization of the emission signal for each activator.  
488 This makes time-resolved spectroscopy an extremely powerful tool for avoiding the  
489 overlapping of various luminescence contributions from REE and other emission centers in  
490 both apatites and other mineral phases.

491 Alternatively, at a constant delay (e.g. just after the laser pulse) one can open the gate  
492 with increasing values from 10 to thousands of ns (here we limit at 450,000 ns just before the  
493 next laser pulse arriving at 500,000 ns at 2 KHz) in order to test the detection of various  
494 emission centers with different lifetimes. This is illustrated in Figure 8 for the Durango  
495 apatite. With short gates (<1,000 ns), only a short lifetime emission signal, here  $\text{Er}^{3+}$ , is  
496 visible in the spectrum because of the less efficient rejection of short lifetime luminescence.  
497 Increasing the gate width allows for the detection of other peaks corresponding to longer  
498 lifetime emission signals from  $\text{Sm}^{3+}$ ,  $\text{Eu}^{3+}$ , and  $\text{Dy}^{3+}$ . This approach is useful for obtaining  
499 neat emission spectra for short lifetime emissions, and also for assessing the rejection  
500 efficiency of the instrumental time resolution.

501 Luminescence spectra retrieved from the synthetic REE-doped hydroxylapatites are  
502 easier to interpret (Figure 4). In the case of  $\text{Eu}^{3+}$ , a strong luminescence signal is observed at



503 all concentrations including the lowest (Figure 4a). This signal is composed of several bands  
504 with two main emission bands centered at 590 and 620 nm corresponding to the  $^5D_0$ - $^7F_1$  and  
505  $^5D_0$ - $^7F_2$  transitions, respectively. Other less important peaks are observed at  $\approx 655$  nm and  $\approx$   
506 570-580 nm and correspond to  $^5D_0$ - $^7F_3$  and  $^5D_0$ - $^7F_0$  transitions, respectively. The case of  $Sm^{3+}$   
507 is very similar to that of  $Eu^{3+}$  with two main emission bands occurring at  $\approx 600$  and 650 nm  
508 (Figure 4b).  $Dy^{3+}$  has no emission bands in any of the spectra even at concentrations as high  
509 as 500 ppm (Figure 4c). It contrasts with natural apatites in which  $Dy^{3+}$  emission bands were  
510 observed at  $\approx 590$  nm (Figure 8). One possible explanation is that emission by  $Dy^{3+}$  is  
511 sensitized either by another REE and/or by  $Mn^{2+}$  in the natural samples. Marfunin (1979) and  
512 Waychunas (2002) have actually reported that  $Mn^{2+}$  can act as a sensitizer for the  
513 luminescence of some REE:  $Mn^{2+}$  absorbs incident energy and transfers it to the REE, which  
514 then emit light. In the case of the synthetic hydroxylapatite,  $Dy^{3+}$  is the only doped element  
515 and therefore is not excited. In the case of  $Nd^{3+}$ , the luminescence peaks are detected only  
516 with a continuous-wave instrument with an excitation at 785 nm in the near infrared part of  
517 the spectrum. This sample could not be studied with the time-resolved instrument (excitation  
518 at 532 nm). The  $Nd^{3+}$  emission is characterized by an intense, broad emission band with  
519 several peaks in the range 850 to 925 nm (Figure 4d).

520

### 521 *Fitting luminescence spectra*

522 A simple visual inspection of the spectra shows that (i) luminescence spectroscopy is  
523 extremely sensitive down to the ppm level and (ii) the overall intensity of the luminescence  
524 signal dramatically increases with the activator concentration. Figure 9 depicts the total  
525 intensity (sum of areas for all peaks after peak fitting) of the luminescence signal for the  
526 emission bands centered at 620 nm and 600 nm as a function of the  $Eu^{3+}$  and  $Sm^{3+}$   
527 concentrations, respectively. In Figure 9, the luminescence signal was analyzed using  
528 continuous-wave spectroscopy and time-resolved spectroscopy with a laser repetition rate of  
529 100 Hz. While in the former case, the excitation/collection is continuous, in the latter case the  
530 signal was mostly generated by a single laser pulse as the signal has almost completely  
531 decayed between two pulses. There is a sharp increase in the luminescence intensity with  
532 increasing concentration of the specific REE. The higher the concentration, the stronger the  
533 luminescence signal is. It is challenging to retrieve any quantitative information from this  
534 observation as the absolute intensity of the signal depends on many other parameters such as  
535 the state of the sample surface, the grain size, the sample effective optical absorption, or the  
536 sample orientation with respect to the incident laser beam.

537           Using the developed Python script, the  $\text{Eu}^{3+}$  and  $\text{Sm}^{3+}$  spectra from the synthetic  
538 hydroxylapatites at different concentrations and different delays of the time sweep  
539 experiments were deconvoluted. For  $\text{Eu}^{3+}$ , the fit was performed on the emission band  
540 centered at 620 nm with 8 bands while it was done on the emission band centered at 600 nm  
541 for  $\text{Sm}^{3+}$  with 5 bands. This is a rather challenging task as these emission bands are likely  
542 generated by a much larger number of electronic transitions. For instance,  $\text{Sm}^{3+}$  luminescence  
543 in apatite results from a large number of f-f electronic transitions. The  $4f^5$  configuration of  
544  $\text{Sm}^{3+}$  ion has at least 73 multiplets yielding 198 energy levels via spin-orbit interactions (Axe  
545 and Dieke, 1962). Not all these transitions are excited and not all of them will generate  
546 emission if excited. The number of bands selected may appear somewhat arbitrary, however it  
547 is determined by what is actually observed in the spectra. First, in both the  $\text{Eu}^{3+}$  and  $\text{Sm}^{3+}$   
548 cases, it was observed that within a specific emission band, all the peaks decay with the same  
549 lifetime. Second, to investigate the effect of the activator concentration, several plots of the  
550 various peaks FWHM or relative intensities were made. In general, no significant trends were  
551 observed except for an increase of the 597 nm/604 nm peak area ratio in the case of  $\text{Sm}^{3+}$ .

552           One purpose of these investigations was to check for possible correlations between  
553 any spectral parameter and the luminescence activator concentration. This would provide a  
554 proxy for quantification or semi-quantification of the activator thanks to its luminescence  
555 signal. No such correlation was found for the spectral parameters. This contrasts with the  $\text{Cr}^{3+}$   
556 luminescence in  $\text{Al}_2\text{O}_3$  quenched glasses doped at various concentrations of  $\text{Cr}^{3+}$ .  $\text{Cr}^{3+}$   
557 luminescence in ruby has been extensively studied and results from optical absorption into the  
558  $^4\text{T}_2$  and  $^2\text{T}_2$  levels and the two well-known emission bands R1 (at 694.25 nm at 300 K) and  
559 R2 (at 692.74 nm at 300 K) originate from the  $^2\text{E}$  level (see Syassen 2008 and references  
560 therein). Chervin et al (2001) studied the spectral parameters of emission spectra of  $\text{Al}_2\text{O}_3$   
561 quenched glasses prepared as micro-spheres doped with various concentrations of  $\text{Cr}^{3+}$  as a  
562 pressure gauge for optically transparent high-pressure diamond anvil cells. They established  
563 clear correlations between the  $\text{Cr}^{3+}$  concentration and the FWHM of both the R1 and R2  
564 emission lines at various excitation energies. The higher the concentration was, the broader  
565 the two lines were. Such correlations can be used as a first-order proxy for  $\text{Cr}^{3+}$  concentration  
566 in ruby glasses.

567           In the case of natural apatites, the situation is even more challenging due to the  
568 multiple overlapping luminescence signals detected in these samples. If time-resolved  
569 spectroscopy can be used to discriminate between short versus long lifetime signals in the  
570 emission spectra, one challenge is that many overlapping REE emission signals have similar

571 lifetimes both amongst themselves and with other emission signals (e.g.  $\text{Mn}^{2+}$ ) making the  
572 fitting of any spectra a challenge.

573

#### 574 *Interpretation of the luminescence lifetime*

575 Time sweep experiments were performed on the natural and synthetic apatites on order to  
576 investigate the lifetime of the  $\text{Eu}^{3+}$  and  $\text{Sm}^{3+}$  emission. For this, the laser repetition rate was  
577 set at 200 Hz. Twenty spectra with a gate of 1 ms were taken with the first being recorded  
578 200  $\mu\text{s}$  after the laser pulse and the delay being augmented by 200  $\mu\text{s}$  for each successive  
579 spectrum with a final spectrum at 4 ms after the pulse. The total intensities of the 8 peaks  
580 composing the emission band at 620 nm for  $\text{Eu}^{3+}$  and of the 5 peaks of the emission band at  
581 600 nm for  $\text{Sm}^{3+}$  are plotted against time (here the delay) as represented in Figure 10. For  
582 both  $\text{Eu}^{3+}$  and  $\text{Sm}^{3+}$ , the higher the concentration of the activator, the faster the decay of the  
583 luminescence. From Figure 10, the luminescence lifetime for each decay curve for  $\text{Eu}^{3+}$  and  
584  $\text{Sm}^{3+}$  can be calculated from equation (4) and plotted against the activator concentration as  
585 shown in Figure 11. In both cases, there is a clear correlation between the luminescence  
586 lifetime and the activator concentration, even at low concentration. The higher the  
587 concentration is, the shorter the luminescence lifetime. Such an acceleration of the decay of  
588 the luminescence signal by increasing the concentration of the activator may be a  
589 consequence of a concentration quenching effect. By increasing the number of activators in  
590 the mineral structure, some activators may directly transfer their excitation energy to a  
591 neighbour activator through a non-radiative process, e.g. by a vibrational process. Such a  
592 correlation has already been observed for other materials like  $\text{Gd}_2\text{O}_3:\text{Eu}^{3+}$  nanocrystals (Meza  
593 et al. 2014). These authors established a clear correlation between the lifetime and  $\text{Eu}^{3+}$   
594 concentration from experimental data that they were able to model using a simple rate  
595 equation model. They interpreted such correlation as the consequence of a concentration  
596 quenching involving energy transfer among  $\text{Eu}^{3+}$  ions but also with  $\text{O}^{2-}$ . Also, as mentioned  
597 above, in hydroxylapatites, part of the de-excitation energy may contribute to some O-H  
598 stretching, which has been seen in deuterated experiments (Al-Kattan et al., 2014).

599 Time sweep experiments were run with the natural apatites in the same configuration  
600 as the one used for the synthetic samples. The  $\text{Eu}^{3+}$  emission band at 620 nm and the  $\text{Sm}^{3+}$   
601 emission band at 600 nm were fitted following the procedure used previously in the case of  
602 the synthetic hydroxylapatites. Time decay figures can be generated for each natural apatite  
603 (not represented here) and the lifetime of  $\text{Eu}^{3+}$  and  $\text{Sm}^{3+}$  emission signals can be calculated.  
604 Several spots were analyzed on each natural apatite in order to have an insight into the intra-

605 sample chemical and structural heterogeneity. Figure 11 depicts all the calculated lifetimes for  
606 both the natural apatites and the synthetic hydroxylapatites for  $\text{Eu}^{3+}$  and  $\text{Sm}^{3+}$  luminescence  
607 versus the concentration in  $\text{Eu}^{3+}$  and  $\text{Sm}^{3+}$  measured by ICP-MS (Table 1 and 2). First of all,  
608 the natural apatites show a systematic, significant dispersion for the calculated lifetimes  
609 compared to synthetic hydroxylapatites. Notably, in the case of  $\text{Eu}^{3+}$ , the concentrations  
610 observed in the natural apatites are lower than those in the synthetic ones (Figure 11a). In  
611 addition, for  $\text{Eu}^{3+}$ , the scattering of the lifetime values for natural apatites covers a range  
612 almost similar to the complete range of lifetime values in the synthetic hydroxylapatites. This  
613 dispersion may reflect the intra-sample chemical zoning for REE, which is often observed in  
614 natural apatites. More generally, there is no clear correlation between the lifetime and the  
615 activator concentration for the natural apatites. The points retrieved from the natural apatites  
616 do not fall on the correlation observed with the synthetic hydroxylapatites. They are generally  
617 above the curve obtained from the synthetic samples, which means that the luminescence  
618 generally takes longer to decay in natural apatites compared to the synthetic hydroxylapatites.

619 A major difference between the natural apatites and synthetic hydroxylapatites is the  
620 presence in the former of several REE activators and even sometimes of other activators like  
621  $\text{Mn}^{2+}$ , while the synthetic hydroxylapatites are doped with a single activator apart from the  
622 minor impurities mentioned above. There is no easy interpretation for this difference in  
623 luminescence behavior but likely there is a complex interplay between the various activators  
624 in the natural samples involving a sensitizing and/or quenching processes for luminescence  
625 among the REE and/or with other activators. For instance, using time-resolved spectroscopy,  
626 Czaja et al. (2010) demonstrated the effective energy transfer between  $\text{Pr}^{3+}$  and  $\text{Sm}^{3+}$  in  
627 natural apatites and showed its effect on the lifetime of emission luminescence from these  
628 crystals. Such effects are absent in the synthetic hydroxylapatites, which are doped with a  
629 single REE activator.

630 As already mentioned by Gaft and Panczer (2013), it is important to distinguish a  
631 theoretical “true” decay time or lifetime from a real effective decay time or lifetime. The true  
632 lifetime is an intrinsic physical parameter of a given transition for an activator in a crystal  
633 lattice in the absence of any non-radiative processes and obtained under precise conditions  
634 (e.g. temperature, pressure). The effective lifetime is the one measured in the laboratory that  
635 can be close to the true one in the case of “perfect” samples with one single activator and no  
636 other impurities. But it can be very different in the case of natural samples. The effective  
637 lifetime is influenced primarily by external parameters like temperature or analytical  
638 parameters, such as the orientation of the crystal with respect to the polarization of the

639 incident laser beam. Also, irradiance may play a role. Overall, as shown by this study, it can  
640 depend on the internal properties of the samples like the presence of other impurities (other  
641 activators, defects), which may trigger complex sensitizing and/or quenching phenomena via  
642 energy transfer.

643

## 644 **Implications**

645 Time-resolved spectroscopy is a very powerful tool which combines both Raman and  
646 luminescence spectroscopy (Figure 7). Time-resolved spectroscopy is extremely efficient in  
647 the detection and identification of REE in accessory mineral such as apatites, other phosphate  
648 minerals, titanite, or zircon. Owing to its capability to scan the time domain and selectively  
649 analyze each emission signal (Figure 7 and 8), time-resolved spectroscopy provides  
650 information that is not accessible to steady-state, *i.e.* continuous-wave, spectroscopy. A major  
651 achievement would be to reach some quantification, or at least semi-quantification of  
652 luminescence activators in mineral phases from the luminescence signal, either directly from  
653 the spectra or through the study of luminescence lifetime. This may be possible in the case of  
654 systems involving one single activator such like  $\text{Cr}^{3+}$  in natural or synthetic ruby, or in our  
655 synthetic REE-doped hydroxylapatites. It is a complex challenge in systems involving more  
656 than one activator as activators are likely to transfer energy among themselves generating  
657 complex quenching and/or sensitizing interactions and thus adding layers of complexity to the  
658 interpretation of the time-resolved data.

659 Currently, the Mars2020 SuperCam time-resolved instrument onboard the NASA  
660 Perseverance rover on Mars should benefit from time-resolved Raman and luminescence  
661 spectroscopy for detecting and investigating REE in phosphate and other minerals in martian  
662 rocks thereby opening new avenues for our understanding of the geochemical processes at  
663 work on this planet (Wiens et al. 2021; Maurice et al. 2021).

664

## 665 **Acknowledgements**

666 The first author was supported by the Labex Matisse (ANR-11-IDEX-0004-02). Funding of  
667 this research by Sorbonne Université and CNRS INP is acknowledged. This paper benefited  
668 from comments by Christoph Lenz and an anonymous reviewer as well as from thorough  
669 reading by Editor Daniel Harlov.

670 **References**

671

- 672 Al-Kattan, A., Santran, V., Dufour, P., Dexpert-Ghys, J., and Drouet, C. (2014) Novel  
673 contributions on luminescent apatite-based colloids intended for medical imaging. *Journal of*  
674 *Biomaterials Applications*, 28, 697-707.
- 675
- 676 Antonakos, A., Liarokapis, E., and Leventouri, T. (2007) Micro-Raman and FTIR studies of  
677 synthetic and natural apatites. *Biomaterials*, 28, 3043–3054.
- 678
- 679 Ashley, K.T., McKeeby, B.E., Harlov, D.E., Bodnar, R.J., and Ramsey, M.S. (2018) High-  
680 Resolution Raman Spectroscopy Constraints on Apatite Halogen Composition: Implications  
681 for Planetary Volcanism and Igneous Processes. Abstract for the Lunar and Planetary Science  
682 Conference, Houston, USA, 1483.
- 683
- 684 Awonusi, A., Morris, M.D., and Tecklenburg, M.M.J. (2007) Carbonate Assignment and  
685 Calibration in the Raman Spectrum of Apatite. *Calcified Tissue International*, 81, 46–52.
- 686
- 687 Axe, J.D., and Dieke, G.H. (1962) Calculation of Crystal - Field Splittings of  $\text{Sm}^{3+}$  and  $\text{Dy}^{3+}$   
688 Levels in  $\text{LaCl}_3$  with Inclusion of J Mixing. *Journal of Chemical Physics*, 37, 2364–2371.
- 689
- 690 Bernard, S., Beyssac, O., and Benzerara, K. (2008) Raman Mapping Using Advanced Line-  
691 Scanning Systems: Geological Applications. *Applied Spectroscopy*, 62, 1180–1188.
- 692
- 693 Beyssac, O. (2020) New trends in Raman spectroscopy: from high-resolution geochemistry to  
694 planetary exploration. *Elements*, 16, 117-122.
- 695
- 696 Blasse, G. (1975) Influence of local charge compensation on site occupation and  
697 luminescence of apatites. *Journal of Solid State Chemistry*, 14, 181–184.
- 698
- 699 Carignan J, Hild P, Mevelle G, Morel J, and Yeghicheyan D (2001) Routine analyses of trace  
700 element in geological samples using flow injection and low pressure on-line liquid  
701 chromatography coupled to ICP-MS: a study of geochemical reference materials BR, DR-N,  
702 UB-N, AN-G and GH. *Geostandards Newsletter*, 25, 187-198.
- 703
- 704 Chervin, J.C., Canny, B., and Mancinelli, M. (2001) Ruby-spheres as pressure gauge for  
705 optically transparent high pressure cells. *High Pressure Research*, 21, 305–314.
- 706
- 707 Choimet, M., Tourrette, A., Marsan, O., Rattu, G., and Drouet, C. (2020) Bio-inspired apatite  
708 particles limit skin penetration of drugs for dermatology applications. *Acta Biomaterialia*,  
709 111, 418-428.
- 710
- 711 Chew, D.M., and Spikings, R.A. (2015) Geochronology and Thermochronology Using  
712 Apatite: Time and Temperature, Lower Crust to Surface. *Elements*, 11, 189–194.
- 713
- 714 Czaja, M., Bodał, S., Lisiecki, R., and Mazurak, Z. (2010) Luminescence properties of  $\text{Pr}^{3+}$   
715 and  $\text{Sm}^{3+}$  ions in natural apatites. *Physics and Chemistry of Minerals*, 37, 425–433.
- 716
- 717 Dubessy, J., Caumon, M-C., Rull, F., and Sharma, S. (2012) Instrumentation in Raman  
718 spectroscopy: Elementary theory and practice. In: Dubessy, J., Caumon, M-C., Rull, F. (eds)

- 719 Raman Spectroscopy Applied to Earth Sciences and Cultural Heritage, p. 83-172, European  
720 Mineralogical Union and Mineralogical Society of Great Britain & Ireland, London.  
721
- 722 Fau, A., Beyssac, O., Gauthier, M., Meslin, P.Y., Cousin, A., Benzerara, K., Bernard, S.,  
723 Boulliard, J.C., Gasnault, O., Forni, O., Wiens, R.C., Morand, M., Rosier, P., Garino, Y.,  
724 Pont, S., and Maurice, S. (2019) Pulsed laser-induced heating of mineral phases: Implications  
725 for laser-induced breakdown spectroscopy combined with Raman spectroscopy.  
726 *Spectrochimica Acta Part B: Atomic Spectroscopy*, 160, 105687.  
727
- 728 Forni, O., Meslin, P.-Y., Drouet, C., Cousin, A., David, G., Mangold, N., Dehouck, E.,  
729 Rampe, E.B., Gasnault, O., Beck, P., Nachon, M., Newsom, H., Blaney, D. L., Clegg, S. M.,  
730 Ollila, A.M., Lasue, J., Maurice, S., and Wiens, R.C. (2020) Apatites in Gale Crater. Abstract  
731 for the Lunar and Planetary Sciences Conference, Houston, USA, 2192.  
732
- 733 Gaft, M., and Panczer, G. (2013) Laser-induced time-resolved luminescence spectroscopy of  
734 minerals: a powerful tool for studying the nature of emission centres. *Mineralogy and  
735 Petrology*, 107, 363–372.  
736
- 737 Gaft, M., Panczer, G., Reisfeld, R., and Uspensky, E. (2001) Laser-induced time-resolved  
738 luminescence as a tool for rare-earth element identification in minerals. *Physics and  
739 Chemistry of Minerals*, 28, 347–363.  
740
- 741 Gaft, M., Reisfeld, R., and Panczer, G. (2015) *Modern Luminescence Spectroscopy of  
742 Minerals and Materials*, 2nd ed, 431 p. Springer International Publishing.  
743
- 744 Gaft, M., Reisfeld, R., Panczer, G., Shoval, S., Champagnon, B., and Boulon, G. (1997)  $\text{Eu}^{3+}$   
745 luminescence in high-symmetry sites of natural apatite. *Journal of Luminescence*, 72–74,  
746 572–574.  
747
- 748 Gomez-Morales, J., Iafisco, M., Delgado-Lopez, J.M., Sarda, S., and Drouet, C. (2013)  
749 Progress on the preparation of nanocrystalline apatites and surface characterization: Overview  
750 of fundamental and applied aspects. *Progress in Crystal Growth and Characterization of  
751 Materials*, 59, 1-46.  
752
- 753 Harlov, D.E. (2015) Apatite: A Fingerprint for Metasomatic Processes. *Elements*, 11, 171–  
754 176.  
755
- 756 Hosseini, S.M., Drouet, C., Al-Kattan, A., and Navrotsky, A. (2014) Energetics of lanthanide-  
757 doped calcium phosphate apatite. *American Mineralogist*, 99, 2320–2327.  
758
- 759 Hughes, J.M., and Rakovan, J. (2002) The Crystal Structure of Apatite,  $\text{Ca}_5(\text{PO}_4)_3(\text{F},\text{OH},\text{Cl})$ .  
760 *Reviews in Mineralogy and Geochemistry*, 48, 1–12.  
761
- 762 Hughes, J.M., and Rakovan, J.F. (2015) Structurally Robust, Chemically Diverse: Apatite and  
763 Apatite Supergroup Minerals. *Elements*, 11, 165–170.  
764
- 765 Jehlička, J., Culka, A., Bersani, D., and Vandenabeele, P. (2017) Comparison of seven  
766 portable Raman spectrometers: beryl as a case study. *Journal of Raman Spectroscopy*, 48,  
767 1289–1299.  
768

- 769 Knutson, C., Peacor, D.R., and Kelly, W.C. (1985) Luminescence, color and fission track  
770 zoning in apatite crystals of the Panasqueira tin-tungsten deposit, Beira-Baixa, Portugal.  
771 American Mineralogist, 70, 829–837.  
772
- 773 Kottaisamy, M., Jagannathan, R., Jeyagopal, P., Rao, R.P., and Narayanan, R. (1994) Eu<sup>2+</sup>  
774 luminescence in M<sub>5</sub>(PO<sub>4</sub>)<sub>3</sub>X apatites, where M is Ca<sup>2+</sup>, Sr<sup>2+</sup> and Ba<sup>2+</sup>, and X is F<sup>-</sup>, Cl<sup>-</sup>, Br<sup>-</sup> and  
775 OH<sup>-</sup>. Journal of Physics D: Applied Physics, 27, 2210–2215.  
776
- 777 Lakowicz, J.R. (2006) Plasmonics in Biology and Plasmon-Controlled Fluorescence.  
778 Plasmonics, 1, 5–33.  
779
- 780 Lenz, C., and Nasdala, L. (2015) A photoluminescence study of REE<sup>3+</sup> emissions in radiation-  
781 damaged zircon. American Mineralogist, 100, 1123–1133.  
782
- 783 Lenz, C., Nasdala, L., Talla, D., Hauzenberger, C., Seitz, R., and Kolitsch, U. (2015) Laser-  
784 induced REE<sup>3+</sup> photoluminescence of selected accessory minerals — An “advantageous  
785 artefact” in Raman spectroscopy. Chemical Geology, 415, 1–16.  
786
- 787 Marfunin, A.S. (1979) Spectroscopy, Luminescence and Radiation Centers in Minerals. 356  
788 p. Springer Verlag Berlin, Heidelberg, New York.  
789
- 790 Maurice, S., Wiens, R.C., Bernardi, P., and others (2021) The SuperCam Instrument suite on  
791 the Mars 2020 Rover: Science objectives and Mast-Unit Description. Space Science Reviews  
792 217, 47.  
793
- 794 McCubbin, F.M., and Jones, R.H. (2015) Extraterrestrial Apatite: Planetary Geochemistry to  
795 Astrobiology. Elements, 11, 183–188.  
796
- 797 Meza, O., Villabona-Leal, E.G., Diaz-Torres, L.A., Desirena, H., Rodríguez-López, J.L., and  
798 Pérez, E. (2014) Luminescence Concentration Quenching Mechanism in Gd<sub>2</sub>O<sub>3</sub>:Eu<sup>3+</sup>. The  
799 Journal of Physical Chemistry A, 118, 1390–1396.  
800
- 801 Mondéjar, S.P., Kovtun, A., and Epple, M. (2007) Lanthanide-doped calcium phosphate  
802 nanoparticles with internal crystallinity and with a shell of DNA as fluorescent probes in cell  
803 experiments. Journal of Materials Chemistry, 17, 4153–4159.  
804
- 805 Morozov, A.M., Morozova, L.G., Trofimov, A.K., and Feofilov, P.P. (1970) Spectral and  
806 luminescent characteristics of fluorapatite single crystals activated by rare-earth ions. Optika i  
807 Spektroskopiya, 29, 1106–1118.  
808
- 809 Nasdala, L., Beyssac, O., William Schopf, J., Bleisteiner, B. (2012) Application of Raman-  
810 based images in the Earth sciences, in: Zoubir, A. (Ed.), Raman Imaging: Techniques and  
811 Applications, p. 145–187, Springer Series in Optical Sciences. Springer Berlin Heidelberg,  
812 Berlin, Heidelberg.  
813
- 814 Nasdala, L., Smith, D.C., Kaindl, R., Ziemann, M.A. (2004) Raman spectroscopy: Analytical  
815 perspectives in mineralogical research, in: Papp, G., Weiszbürg, T.G., Beran, A., Libowitzky,  
816 E. (Eds.), Spectroscopic Methods in Mineralogy p. 281–343. Mineralogical Society of Great  
817 Britain and Ireland, Germany.  
818



- 819 O'Shea, D.C., Bartlett, M.L., and Young, R.A. (1974) Compositional analysis of apatites with  
820 Laser-Raman spectroscopy: (OH,F,Cl)apatites. Archives of Oral Biology, 19, 995–1006.  
821
- 822 Panczer, G., De Ligny, D., Mendoza, C., Gaft, M., Seydoux-Guillaume, A.-M., Wang, X.  
823 (2012) Raman and fluorescence. In: Dubessy, J., Caumon, M-C., Rull, F. (eds) Raman  
824 Spectroscopy Applied to Earth Sciences and Cultural Heritage, p. 61-82, European  
825 Mineralogical Union and Mineralogical Society of Great Britain & Ireland, London.  
826
- 827 Panczer, G., Gaft, M., Reisfeld, R., Shoval, S., Boulon, G., and Champagnon, B. (1998)  
828 Luminescence of uranium in natural apatites. Journal of Alloys and Compounds, 275–277,  
829 269–272.  
830
- 831 Pasteris, J.D., and Beyssac, O. (2020) Welcome to Raman Spectroscopy: Successes,  
832 Challenges, and Pitfalls. Elements, 16, 87-92.  
833
- 834 Rakovan, J.F., and Pasteris, J.D. (2015) A Technological Gem: Materials, Medical, and  
835 Environmental Mineralogy of Apatite. Elements, 11, 195–200.  
836
- 837 Reisfeld, R., Gaft, M., Boulon, G., Panczer, C., and Jørgensen, C.K. (1996) Laser-induced  
838 luminescence of rare-earth elements in natural fluor-apatites. Journal of Luminescence, 69,  
839 343–353.  
840
- 841 Rey, C., Marsan, O., Combes, C., Drouet, C., Grossin, D., and Sarda, S. (2014)  
842 Characterization of Calcium Phosphates Using Vibrational Spectroscopies. In: Ben-Nissan B.  
843 (ed) Advances in Calcium Phosphate Biomaterials p. 229-266. Springer Series in  
844 Biomaterials Science and Engineering, vol 2. Springer, Berlin, Heidelberg.  
845
- 846 Suarez C.A., Machpherson G.L., González L.A., and Grandstaff D.E. (2010) Heterogeneous  
847 rare earth element (REE) patterns and concentrations in a fossil bone: Implications for the use  
848 of REE in vertebrate taphonomy and fossilization history. Geochimica and Cosmochimica  
849 Acta 74, 2970-2988.  
850
- 851 Sun, S.-S. and McDonough, W.-S. (1989) Chemical and isotopic systematics of oceanic  
852 basalts: implications for mantle composition and processes. Geological Society, London,  
853 Special Publications, 42, 313-345.  
854
- 855 Syassen, K. (2008) Ruby under pressure. High Pressure Research, 28, 75-126.  
856
- 857 Waychunas, G.A. (2014) Luminescence Spectroscopy. Reviews in Mineralogy and  
858 Geochemistry, 78, 175–217.  
859
- 860 Waychunas, G.A. (2002) Apatite Luminescence. Reviews in Mineralogy and Geochemistry,  
861 48, 701–742.  
862
- 863 Webster, J.D., and Piccoli, P.M. (2015) Magmatic Apatite: A Powerful, Yet Deceptive,  
864 Mineral. Elements, 11, 177–182.  
865
- 866 Wiens, R.C., Maurice, S., Robinson, S.H., and others (2021) The SuperCam Instrument Suite  
867 on the NASA Mars 2020 Rover: Body Unit and Combined System Tests. Space Science  
868 Reviews 217, 4.

869 **Figures Caption**

870

871 **Figure 1:** Chondrite-normalized REE patterns from ICP-MS analysis of natural apatites  
872 (normalization factor from Sun and McDonough, 1989).

873

874 **Figure 2:** XRD diffractograms for the synthetic hydroxylapatites doped with Eu at increasing  
875 concentration (see Table 2 for measured concentration). Similar crystallinity was obtained for  
876 the other samples doped with Sm, Dy and Nd.

877

878 **Figure 3:** Fourier Transform Infrared spectra for synthetic hydroxylapatites doped with Eu at  
879 increasing concentrations (see Table 2 for measured concentrations). Similar crystallinity was  
880 obtained for the other samples doped with other with Sm, Dy and Nd.

881

882 **Figure 4:** Representative continuous-wave Raman and luminescence spectra of synthetic  
883 hydroxylapatites doped with Eu (a), Sm (b), Dy (c), and Nd (d). All spectra are raw data,  
884 excitation at 532 nm except for Nd (785 nm) and are acquired with the same acquisition time  
885 for each series. Note the strong background affecting the spectrum Sm2. R indicates a Raman  
886 peak.

887

888 **Figure 5:** Representative Raman spectra obtained on an hydroxylapatite doped with 23,936  
889 ppm of Sm. The continuous-wave spectrum was obtained with the time-resolved instrument  
890 by opening the gate for 450,000 ns (nearly pulse to pulse at 2 KHz) and including the laser  
891 pulse. The luminescence signal from Sm significantly masks the Raman signal. The time-  
892 resolved spectrum was obtained with the time-resolved instrument by opening the gate for 5  
893 ns including the laser pulse. The luminescence signal from Sm is completely rejected and the  
894 Raman signal is clearly visible.

895

896 **Figure 6:** Representative continuous-wave (green, ICCD gate of 450,000 ns including the  
897 laser pulse) and time-resolved (red, ICCD gate of 5 ns centered on the laser pulse) Raman  
898 spectra of some natural apatites. All spectra are raw data.

899

900 **Figure 7:** Time-resolved Raman and luminescence spectra obtained on the Durango apatite  
901 by using various combinations of delay and gates for the ICCD. From top to bottom green  
902 (Raman + all luminescence) is obtained with a long gate (450,000 ns) including the laser

903 pulse. Red (Raman only) is obtained with a short gate (5 ns) including the laser pulse. Black  
904 (all luminescence, no Raman) is obtained with a long gate (450,000 ns) opened just after the  
905 laser pulse (10 ns). Pale grey (short lifetime luminescence) is obtained with a gate of 1,500 ns  
906 opened just after the laser pulse (5 ns). Dark grey (long lifetime luminescence) is obtained  
907 with a long gate (450,000 ns) opened 1,500 ns after the laser pulse.

908

909 **Figure 8:** Time-resolved luminescence spectra obtained on the Durango apatite by using a  
910 constant delay (laser pulse not included so no Raman) and increasing progressively the  
911 opening of the ICCD gate.

912

913 **Figure 9:** Diagrams showing the area of the luminescence bands versus the doping element  
914 concentration for the 620 nm emission band for Eu (a) and the 600 nm emission band for Sm  
915 (b). The grey inset zooms on the same diagram at low concentration (<3,000 ppm).

916

917 **Figure 10:** Result of the time-sweep experiment for Eu- and Sm-doped hydroxylapatites (see  
918 Table 2 for the measured concentration). The plots depict the normalized intensity of the 620  
919 nm emission band for Eu (a) and 600 nm emission band for Sm (b) versus the delay of the  
920 ICCD gate. This figure illustrates the time decay of the luminescence signal for Eu (a) and Sm  
921 (b). Lifetime is calculated as the slope of the line going through the experimental points.

922

923 **Figure 11:** Compilation of the lifetime of the luminescence for Eu (a) and Sm (b) versus the  
924 concentration in activator Eu and Sm, respectively, for the synthetic REE-doped (black  
925 circles) and natural apatites (colored squares).

926

927

928

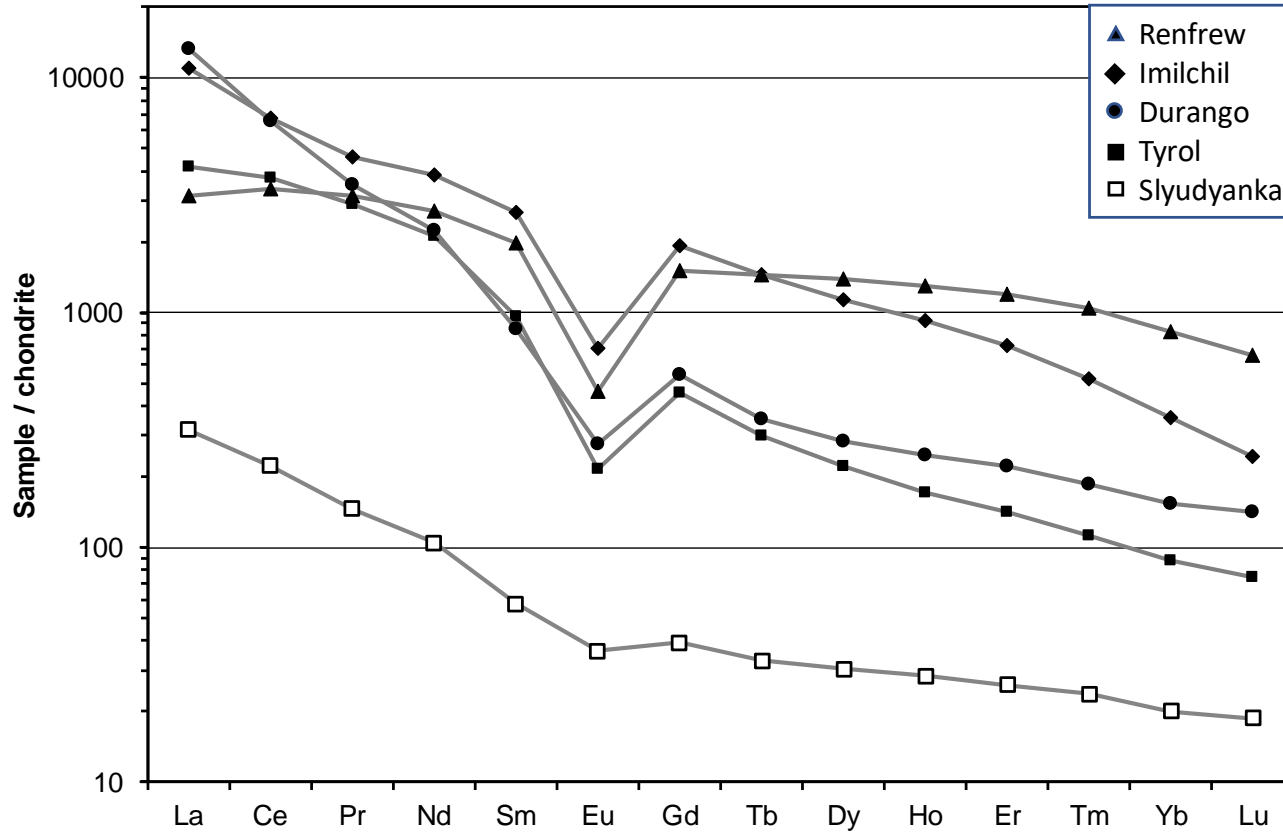


Figure 1

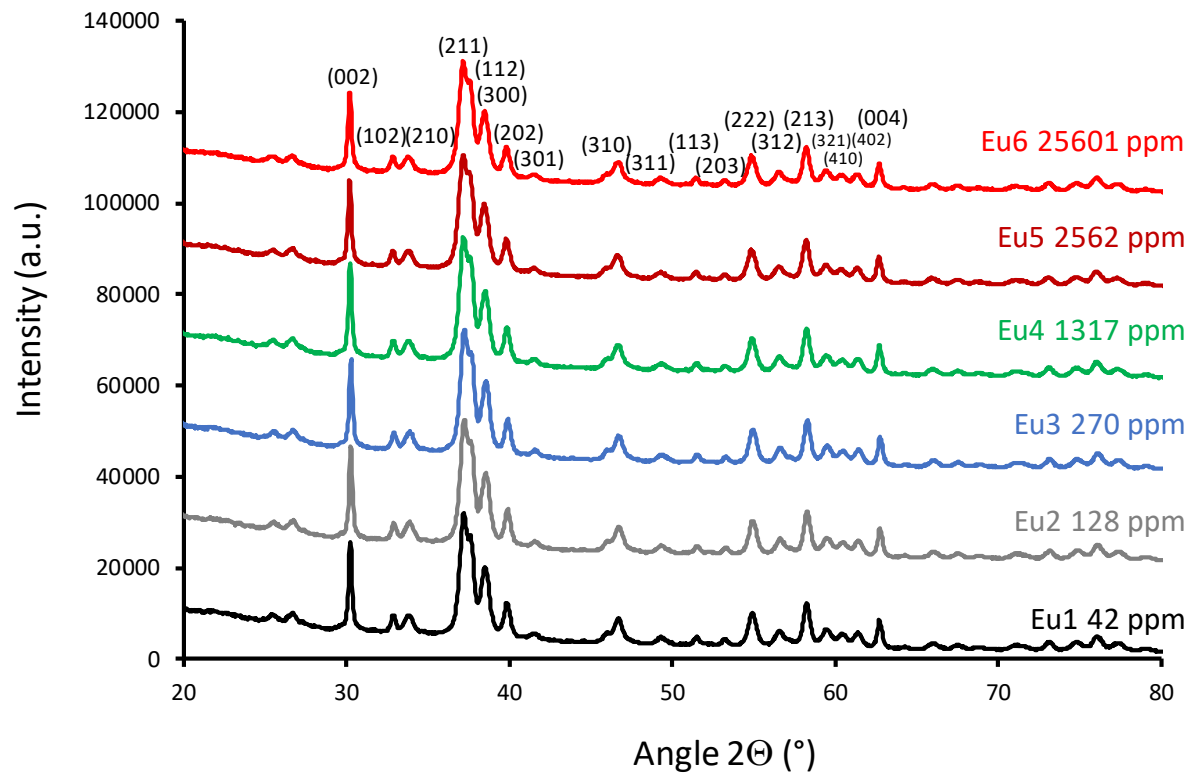


Figure 2

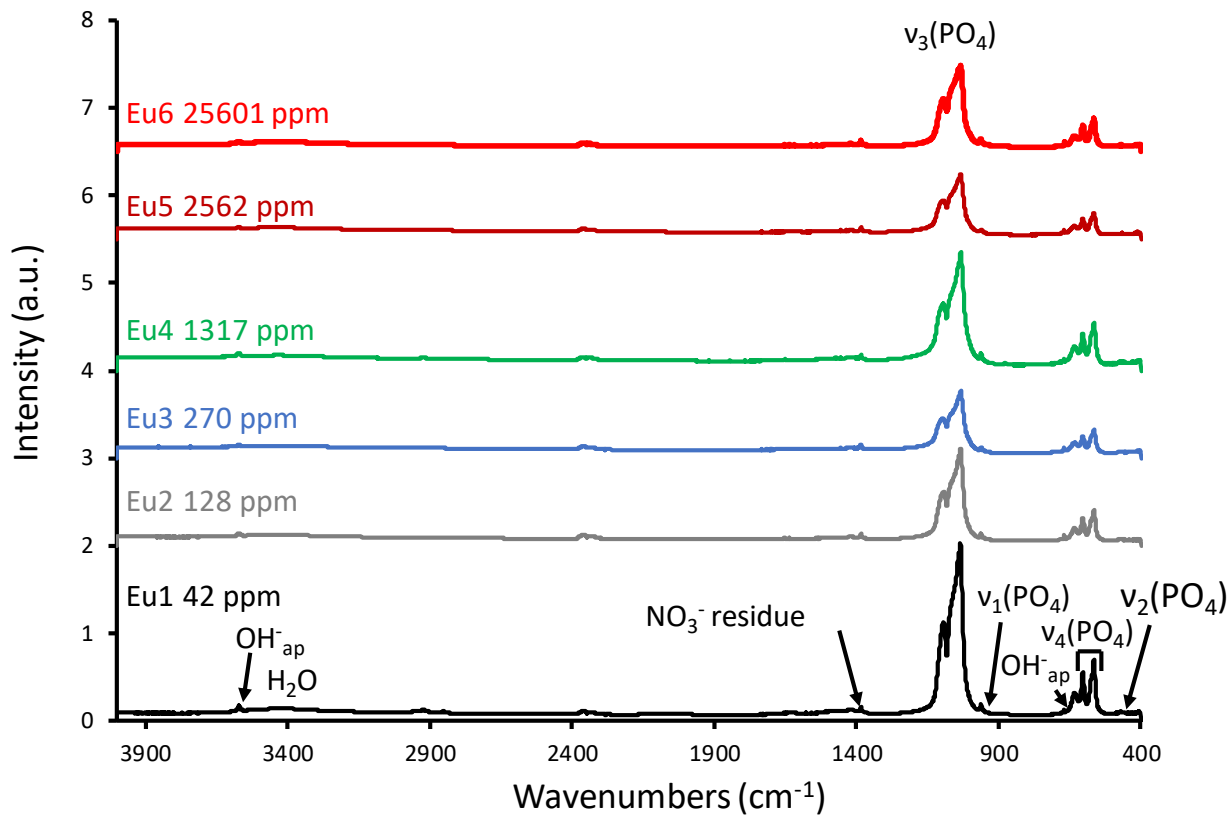


Figure 3

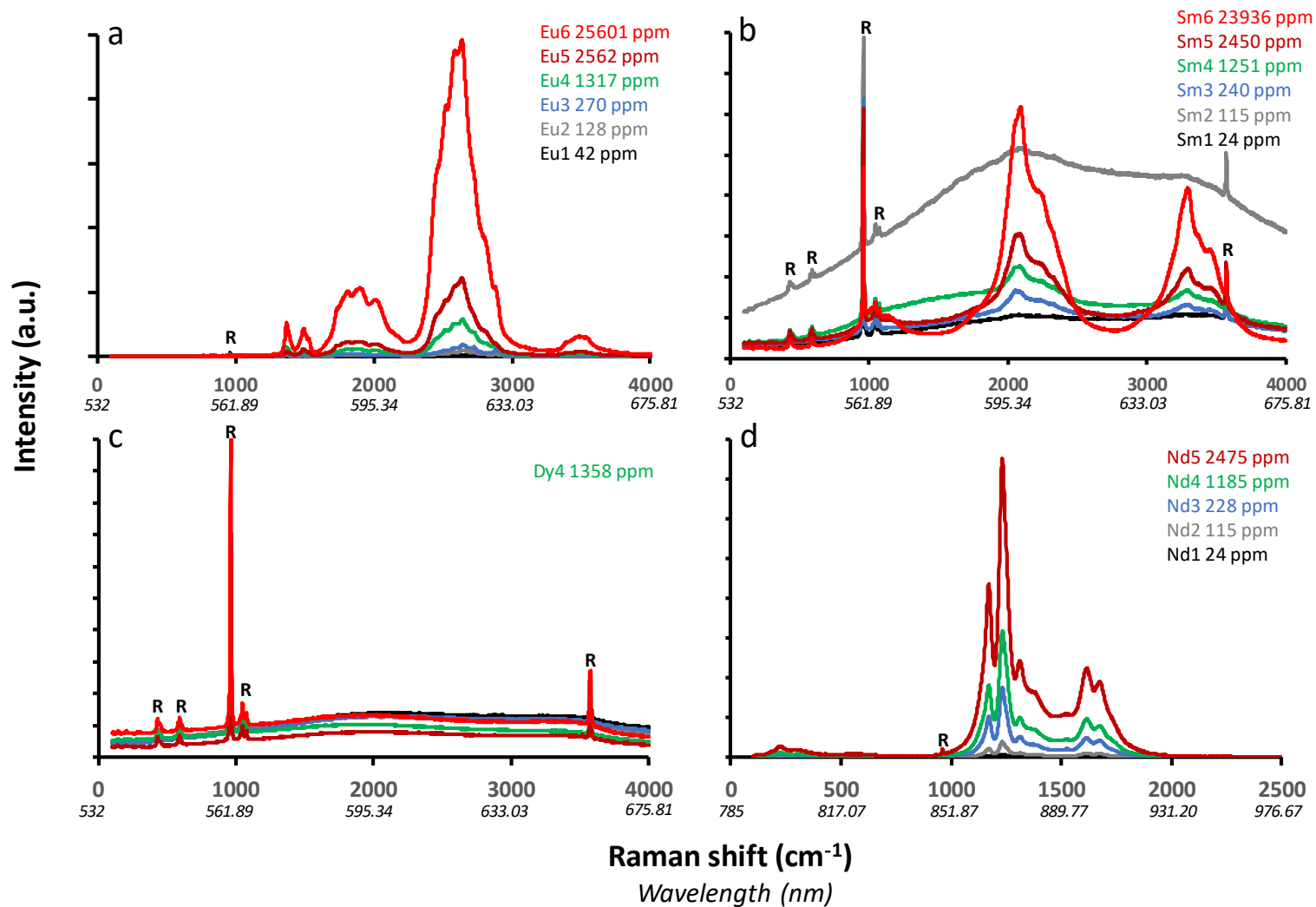


Figure 4

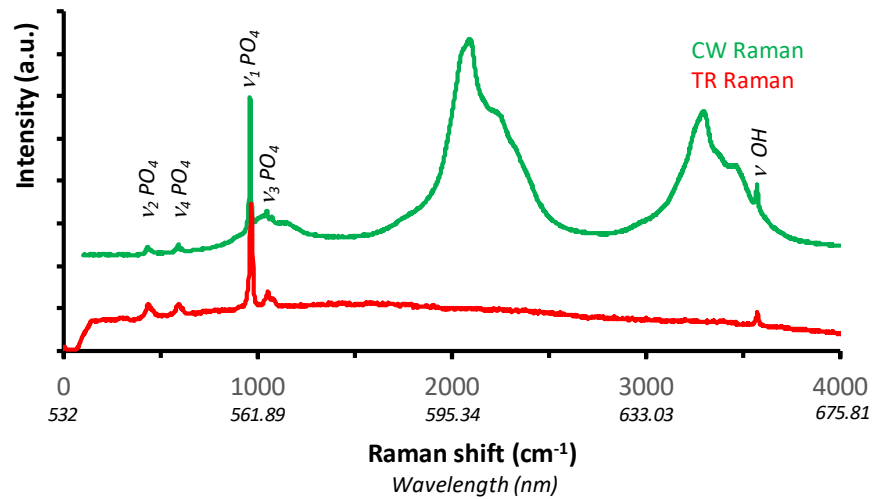


Figure 5



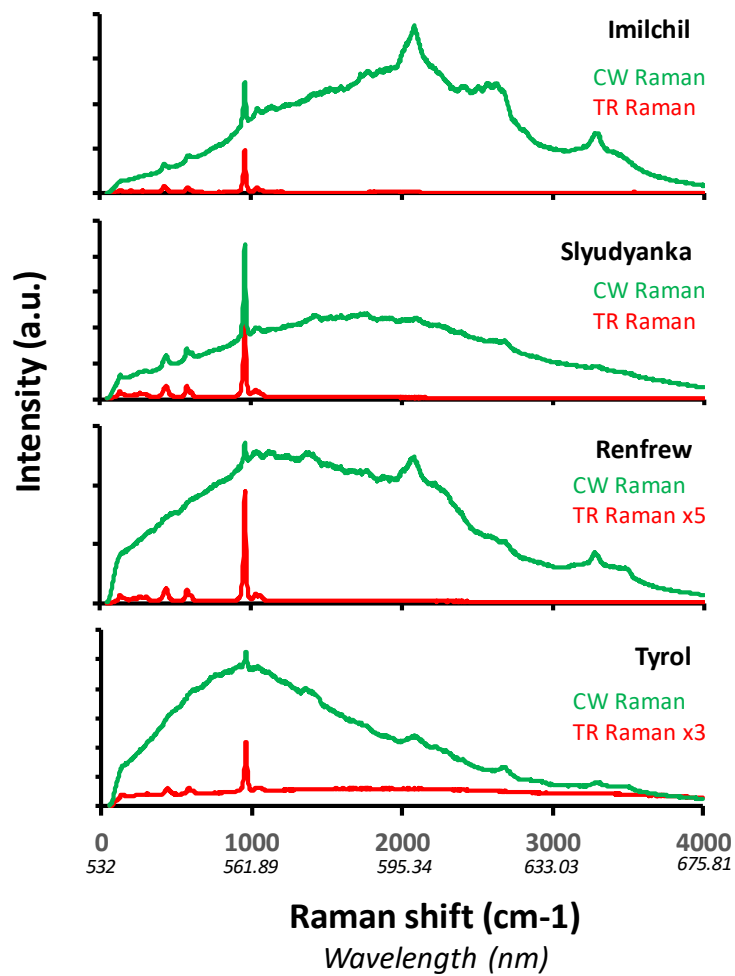


Figure 6

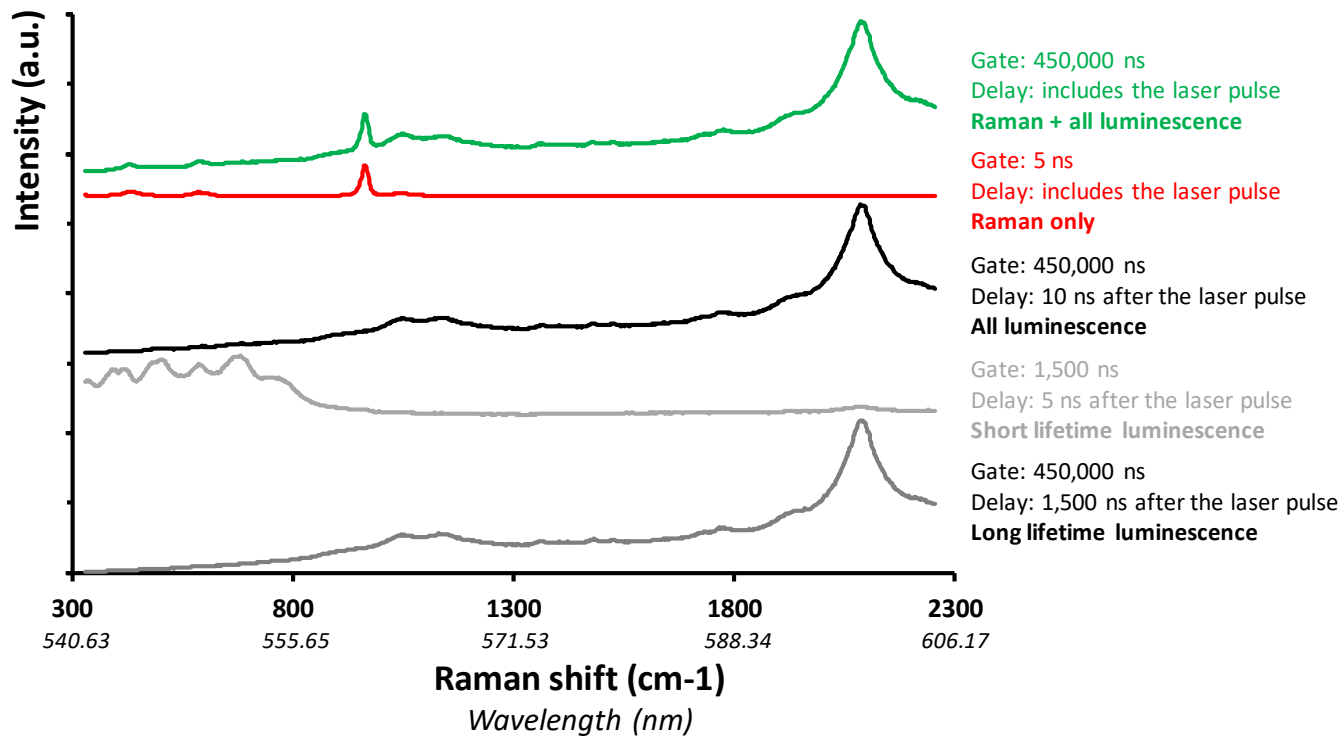


Figure 7

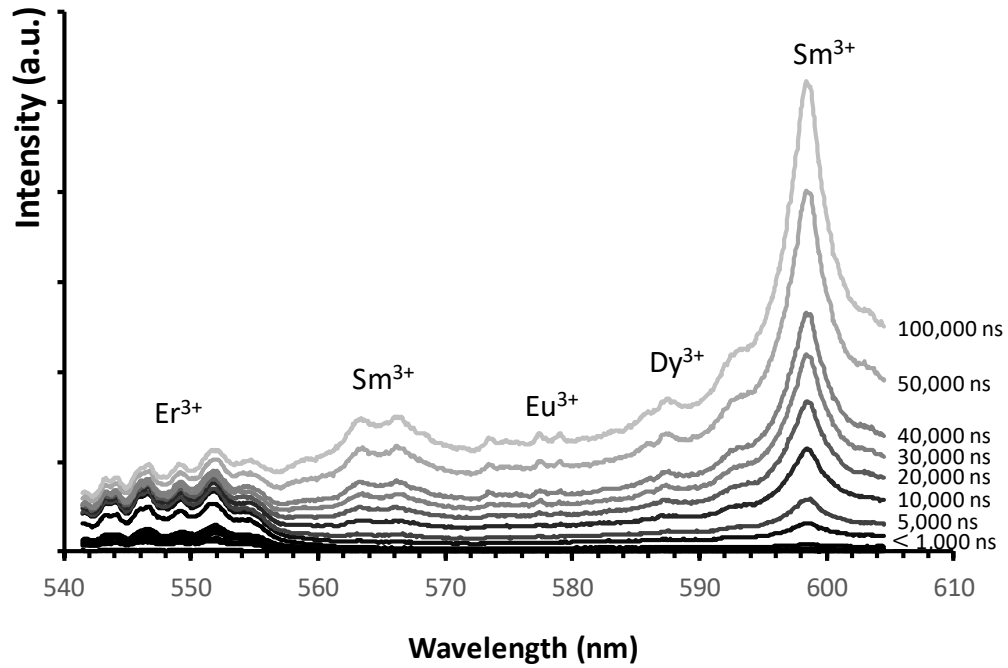


Figure 8

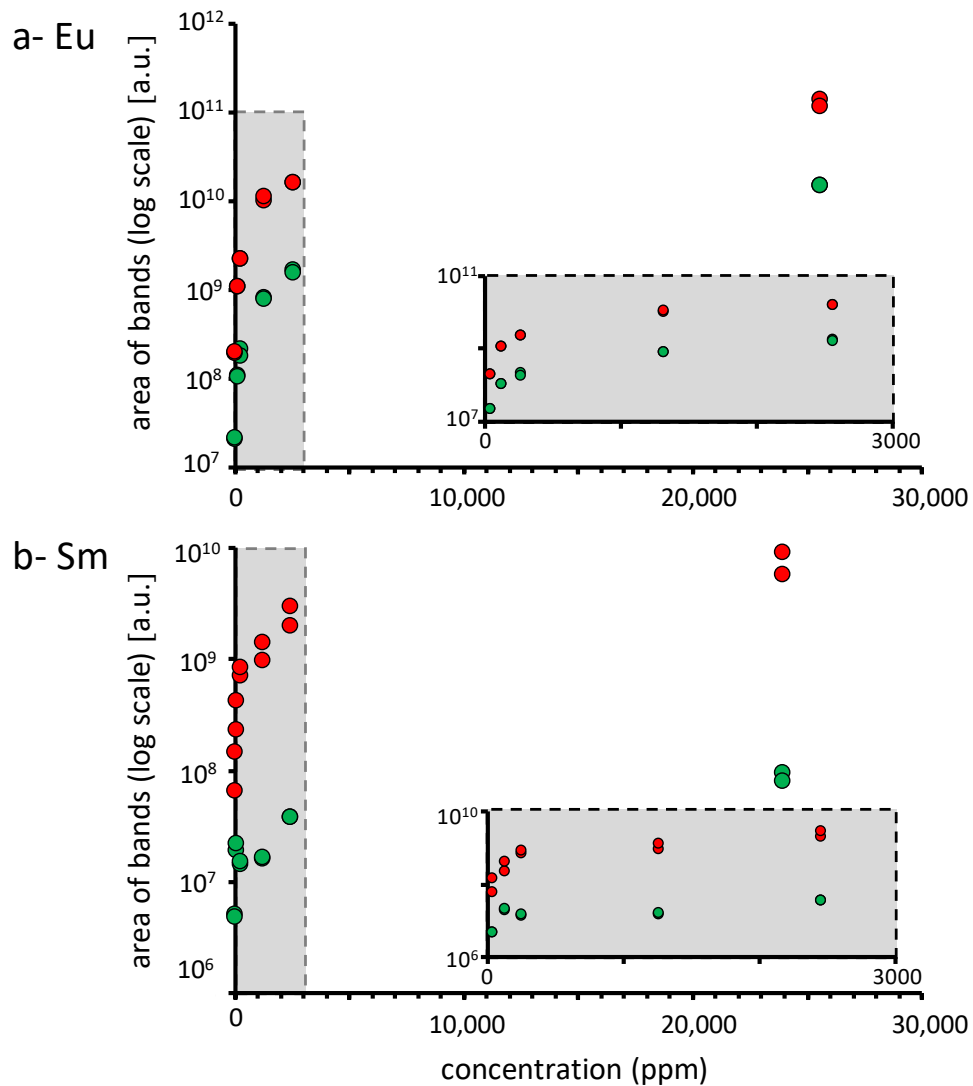


Figure 9

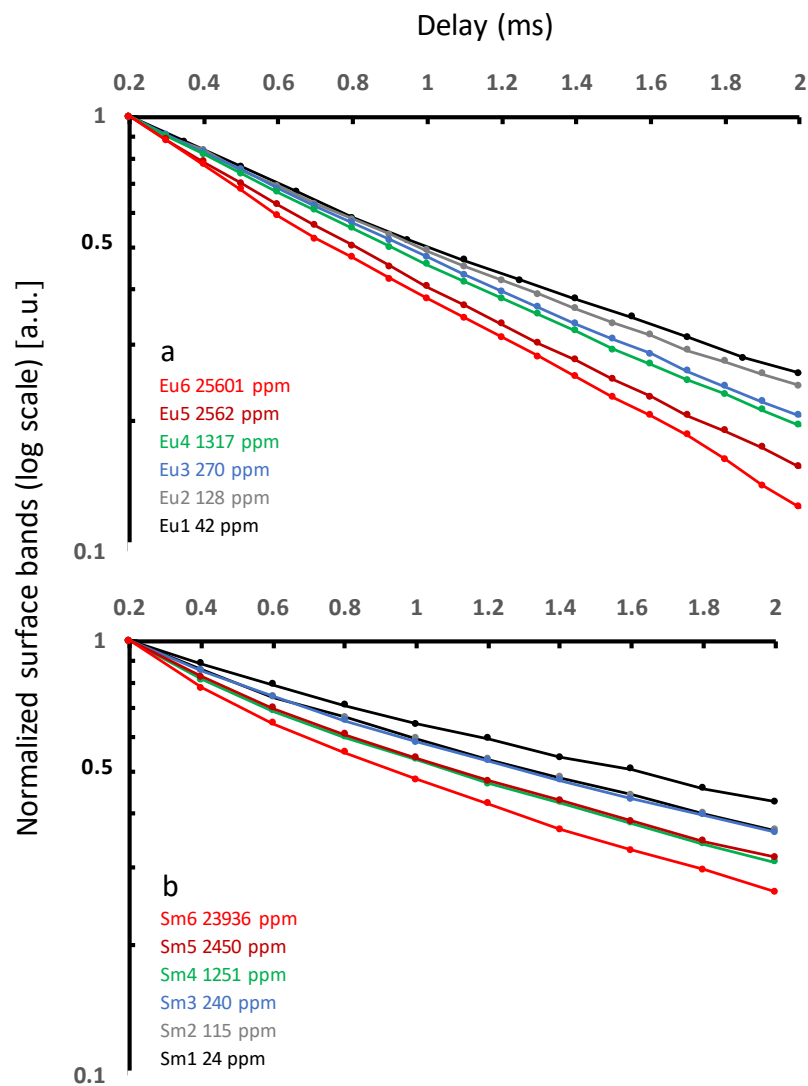


Figure 10

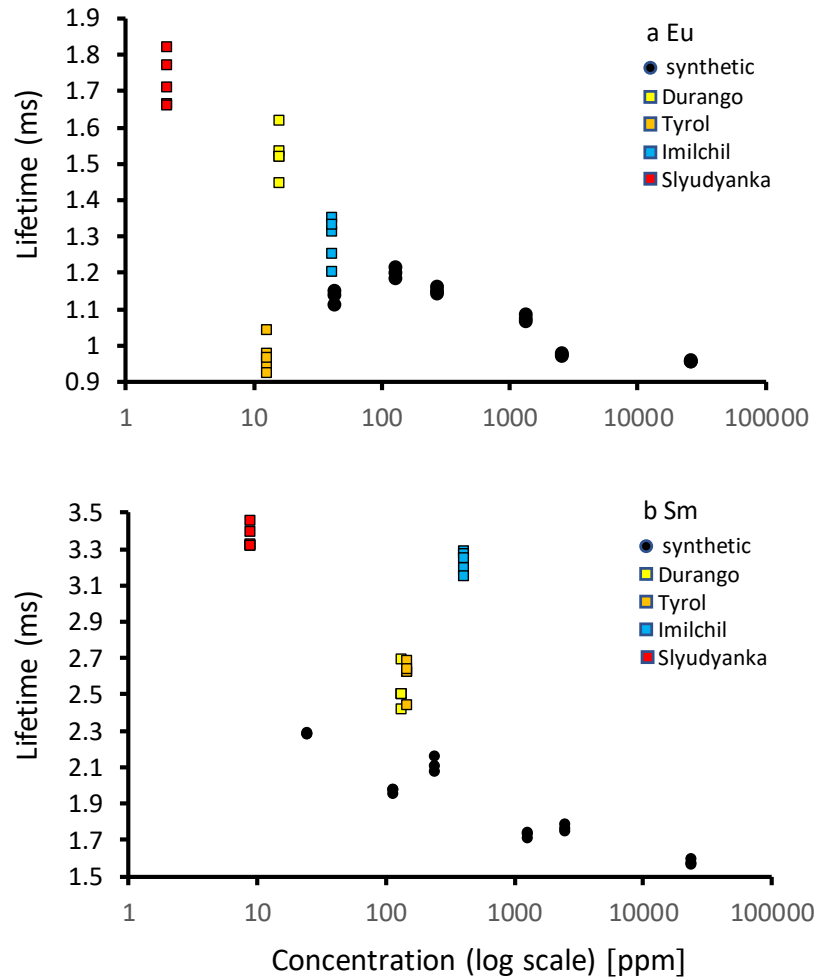


Figure 11

**Table 1:** Nd, Sm, Eu and Dy composition of the synthetic hydroxyapatite samples measured by ICP-MS. ( $\mu\text{g/g}$  = ppm; < L.D below limit of detection).

<b>Sample reference</b>	<b>Nd</b> $\mu\text{g/g}$	<b>Sm</b> $\mu\text{g/g}$	<b>Eu</b> $\mu\text{g/g}$	<b>Dy</b> $\mu\text{g/g}$	<b>CaO</b> wt%	<b>P<sub>2</sub>O<sub>5</sub></b> wt%
<b>Eu 1</b>	0	0	42	0	53.02	39.01
<b>Eu 2</b>	0	0	128	0	53.06	38.92
<b>Eu 3</b>	0	< L.D.	270	0	53.34	39.36
<b>Eu 4</b>	0	0	1 317	0	52.80	38.63
<b>Eu 5</b>	0	0	2 562	0	52.33	37.87
<b>Eu 6</b>	0	0	25 601	0	50.02	37.36
<b>Sm 1</b>	0	24	5	0	52.77	39.17
<b>Sm 2</b>	0	115	5	0	52.06	37.89
<b>Sm 3</b>	0	240	1	0	53.31	39.82
<b>Sm 4</b>	0	1 251	0	0	52.35	38.47
<b>Sm 5</b>	0	2 450	0	0	52.37	38.31
<b>Sm 6</b>	0	23 936	1	1	50.06	37.13
<b>Nd 1</b>	24	4	< L.D.	0	52.91	38.83
<b>Nd 2</b>	115	1	< L.D.	0	52.46	38.14
<b>Nd 3</b>	228	0	< L.D.	1	52.81	38.84
<b>Nd 4</b>	1 185	3	2	2	53.16	39.03
<b>Nd 5</b>	2 475	0	0	5	52.57	38.45
<b>Nd 6</b>	24 832	2	1	50	50.59	39.91
<b>Dy 4</b>	4	< L.D.	0	1 358	51.89	38.16

**Table 2:** Major elements (oxide wt%) and REE composition ( $\mu\text{g/g}$  or ppm) of the natural apatite samples measured by ICP-MS (< L.D below limit of detection).

	<b>Tyrol</b>	<b>Imilchil</b>	<b>Renfrew</b>	<b>Slyudyanka</b>	<b>Durango</b>
<b>Location</b>	Tyrol – Austria	Imilchil – Morocco	Renfrew, Ontario – USA	Lake Baikal, Russia	Durango – Mexico
<b>Type</b>	fluorapatite	fluorapatite	fluorapatite	unknown	fluorapatite
<b>Form</b>	polycrystal	polycrystal	polycrystal	polycrystal	monocrystal
<b>Color</b>	dark green	light green – yellow	light green	light blue	yellow
<b>CaO</b>	53.23	53.35	54.11	54.34	53.58
<b>P<sub>2</sub>O<sub>5</sub></b>	39.83	41.47	40.72	39.92	40.68
<b>MnO</b>	< L.D.	0.02	0.11	< L.D.	< L.D.
<b>Sc</b>	2	1	1	< L.D.	1
<b>Y</b>	297	1418	1643	46	452
<b>La</b>	992	2590	741	75	3166
<b>Ce</b>	2290	4138	2058	136	4030
<b>Pr</b>	276	438	297	14	332
<b>Nd</b>	994	1794	1264	49	1045
<b>Sm</b>	147	407	302	9	131
<b>Eu</b>	13	41	27	2	16
<b>Gd</b>	94	397	308	8	112
<b>Tb</b>	11	54	55	1	13
<b>Dy</b>	56	286	353	8	72
<b>Ho</b>	10	52	74	2	14
<b>Er</b>	23	119	197	4	37
<b>Tm</b>	3	13	27	1	5
<b>Yb</b>	15	61	141	3	26
<b>Lu</b>	2	6	17	0	4